

Numerical Simulations of Gaseous Disks Generated from Collisional Cascades at the Roche Limits of White Dwarf Stars

Scott J. Kenyon

Smithsonian Astrophysical Observatory, 60 Garden Street, Cambridge, MA 02138

e-mail: skenyon@cfa.harvard.edu

Benjamin C. Bromley

Department of Physics & Astronomy, University of Utah, 201 JFB, Salt Lake City, UT 84112

e-mail: bromley@physics.utah.edu

ABSTRACT

We consider the long-term evolution of gaseous disks fed by the vaporization of small particles produced in a collisional cascade inside the Roche limit of a $0.6 M_{\odot}$ white dwarf. Adding solids with radius r_0 at a constant rate \dot{M}_0 into a narrow annulus leads to two distinct types of evolution. When $\dot{M}_0 \gtrsim \dot{M}_{0,crit} \approx 3 \times 10^4 (r_0/1 \text{ km})^{3.92} \text{ g s}^{-1}$, the cascade generates a fairly steady accretion disk where the mass transfer rate of gas onto the white dwarf is roughly \dot{M}_0 and the mass in gas is $M_g \approx 2.3 \times 10^{22} (\dot{M}_0/10^{10} \text{ g s}^{-1}) (1500 \text{ K}/T_0) (10^{-3}/\alpha) \text{ g}$, where T_0 is the temperature of the gas near the Roche limit and α is the dimensionless viscosity parameter. If $\dot{M}_0 \lesssim \dot{M}_{0,crit}$, the system alternates between high states with large mass transfer rates and low states with negligible accretion. Although either mode of evolution adds significant amounts of metals to the white dwarf photosphere, none of our calculations yield a vertically thin ensemble of solids inside the Roche limit. X-ray observations can place limits on the mass transfer rate and test this model for metallic line white dwarfs.

Subject headings: planetary systems – planets and satellites: formation – planets and satellites: physical evolution – planets and satellites: rings – stars: circumstellar matter – stars: white dwarfs

1. INTRODUCTION

Over the past four decades, observations have shown that many white dwarfs have metallic absorption lines from O, Mg, Al, Si, Ca, Fe, and a variety of other elements with atomic number $Z \geq 6$ (e.g., Shipman et al. 1977; Cottrell & Greenstein 1980; Shipman & Greenstein 1983; Lacombe et al. 1983; Liebert et al. 1987; Kenyon et al. 1988; Sion et al. 1990; Zuckerman & Reid 1998; Jura & Young 2014; Koester et al. 2014; Kepler et al. 2016; Xu et al. 2017, and references therein). Some of these stars have near-IR excess emission from warm dust orbiting near the Roche limit (e.g., Kilic et al. 2005; Reach et al. 2005; Hansen et al. 2006; Tremblay & Bergeron 2007; von Hippel et al. 2007; Farihi et al. 2009; Girven et al. 2011; Debes et al. 2011; Chu et al. 2011; Barber et al. 2012; Hoard et al. 2013; Barber et al. 2014; Bergfors et al. 2014; Rocchetto et al. 2015; Farihi 2016; Bonsor et al. 2017). A few have metallic emission features from ionized or neutral gas, also orbiting within the Roche limit (e.g., Gänsicke et al. 2006, 2007, 2008; Melis et al. 2010; Farihi et al. 2012; Melis et al. 2012; Debes et al. 2012a; Wilson et al. 2014).

Currently popular models for these white dwarfs propose that the photospheric absorption lines result from accretion of solid material originally orbiting at large distances from the host star (e.g., Alcock & Illarionov 1980; Lacombe et al. 1983; Alcock et al. 1986; Jura 2003; Koester & Wilken 2006; Jura et al. 2007a,b; Wyatt et al. 2014; Veras 2016). Perturbations of the orbits lead to a succession of solids that fall within the Roche limit of the white dwarf and eventually form an optically thick, vertically thin disk surrounding the white dwarf. Vaporization of disk particles produces a gaseous disk, which moderates direct accretion of material onto the white dwarf photosphere (e.g., Debes & Sigurdsson 2002; Jura 2003, 2008; Rafikov 2011a; Debes et al. 2012b; Metzger et al. 2012; Veras et al. 2013; Brown et al. 2017).

In Kenyon & Bromley (2017, hereafter KB2017), we considered the long-term evolution of solid material placed on mildly eccentric ($e = 0.01$) orbits within a narrow annulus near the Roche limit of a $0.6 M_{\odot}$ white dwarf. Destructive collisions generate a collisional cascade which converts 1–100 km asteroids into dust grains with radii $r \lesssim 1 \mu\text{m}$. When solids are replenished at a rate \dot{M}_0 , the system often finds an equilibrium which depends on \dot{M}_0 and r_0 the radius of the largest solid added to the annulus. Equilibria with constant mass require $r_0 \lesssim 10\text{--}30$ km and $\dot{M}_0 \gtrsim 10^7\text{--}10^8 \text{ g s}^{-1}$. Otherwise, the solid mass in the annulus oscillates between high states with large collision rates and low states with negligible collision rates.

Throughout all of our simulations, the vertical scale height H of the solids remains large, $H \approx 0.01a$, where a is the distance of the annulus from the central star. In principle, collisional damping is sufficient to reduce H significantly on 5–10 collision times. In practice, however, the collisional cascade processes solids on shorter time scales and prevents damping. Thus, collisional processes are incapable of assembling a thin disk of solids inside the Roche

limit of a white dwarf.

Although simple order-of-magnitude estimates suggest that interactions between the solids and the gas are also incapable of reducing H (KB2017), it is necessary to consider whether a more detailed treatment of the gas can produce conditions more amenable to the formation of a thin disk of solids. Here, we expand on KB2017 and derive the time evolution of a gaseous disk formed by the vaporization of small solids produced in the collisional cascade. Once we infer the radial distribution of the gas surface density (Σ_g), we use an adopted temperature distribution to calculate the impact of the gas on solid particles.

In addition to placing better constraints on the ability of solids to collapse into a thin disk, we derive the time evolution of the accretion rate of gas onto the central white dwarf. These results allow us to begin to compare theoretical estimates of accretion rates with observations.

After briefly summarizing the algorithms used in our simulations (§2), we describe results for a suite of calculations with different r_0 and \dot{M}_0 (§3). We then compare our results with previous investigations, discuss the likely impact of the gas on solid particles, and make some initial comparisons with observations (§4). We conclude with a brief summary (§5).

2. THEORETICAL BACKGROUND

To follow the evolution of a gaseous disk generated from vaporized solids, we rely on *Orchestra*, a parallel C++/MPI hybrid coagulation + n -body code that tracks the accretion, fragmentation, and orbital evolution of solid particles ranging in size from a few microns to thousands of km (Kenyon & Bromley 2001, 2004, 2008; Bromley & Kenyon 2011a,b; Kenyon & Bromley 2016). The ensemble of codes within *Orchestra* includes a multi-annulus coagulation code for small particles, an n -body code for large particles, and separate radial diffusion codes for solids and gas. Several algorithms link the codes together, enabling each component to react to the evolution of other components.

As in KB2017, we assume solid particles lie within a single annulus of width Δa at a distance a_0 from a central star with mass $M_\star = 0.6 M_\odot$ and radius $R_\star = 0.013 R_\odot$ ($a_0 = 1.16 R_\odot$; $\Delta a = 0.2a_0$). Particles on circular orbits have velocities $v_K = (GM_\star / a_0)^{1/2} \approx 300 \text{ km s}^{-1}$. Within the annulus, there are M mass batches with characteristic mass m_i and logarithmic spacing $\delta = m_{i+1}/m_i$; adopting $\delta = 1.4$ provides a reasonably accurate solution for the cascade (e.g, Kenyon & Bromley 2015a,b, 2016, and references therein). Batches contain N_i particles with total mass M_i , average mass $\bar{m}_i = M_i/N_i$, horizontal velocity h_i ($e_i = \sqrt{1.6}h_i/v_K$), and vertical velocity v_i ($\sin i = \sqrt{2}v_i/v_K$). The number of particles, total

mass, and orbital velocity of each batch evolve through physical collisions and gravitational interactions with all other mass batches in the ring.

At the start of each calculation, the single annulus is empty of solids. During a time step of length Δt , we add a mass in solids, $\delta M = \dot{M}_0 \Delta t$. Every solid particle added to the annulus has radius r_0 , mass m_0 , eccentricity e_0 , and inclination i_0 . The solids have a mass density $\rho_s = 3 \text{ g cm}^{-3}$. Along with the input rate \dot{M}_0 , the initial properties of the solids are held fixed in each calculation. The number of particles added to the grid is $\Delta N = \dot{M}_0 \Delta t / m_0$. Our algorithm uses a random number generator to round ΔN up or down to the nearest integer. For systems with large r_0 , this procedure introduces some shot noise into the input rate.

When the solid mass reaches a critical level, the particles begin to collide. As summarized in KB2017, the coagulation code within *Orchestra* derives the rates and outcomes of physical collisions and the velocity evolution from gravitational interactions among all particles in the grid. By setting $e_0 = 0.01$ and $i_0 = e_0/2$, we ensure that all collisions are destructive, with approximate collision velocities $v_c \approx e_0 v_K \approx 3 \text{ km s}^{-1}$. The complete ensemble of destructive collisions generates a collisional cascade, where solids with initial radii of 1–100 km are gradually ground into $1 \text{ }\mu\text{m}$ dust grains.

In KB2017, we assumed that particles with radii $r \lesssim 1 \text{ }\mu\text{m}$ were vaporized and ‘lost’ to the system. Here, we consider how this material evolves when it feeds a gaseous reservoir. Vaporized solids are placed into the reservoir at a rate \dot{M}_v , which is derived from the coagulation code every time step. This material is spread evenly over the width of the annulus, which extends from an inner radius $a_{in} = a_0 - \Delta a/2$ to an outer radius $a_{out} = a_0 + \Delta a/2$. Between a_{in} and a_{out} , the reservoir grows in surface density at a rate $\dot{\Sigma}_g = \dot{M}_v / 2\pi a_0 \Delta a$.

As the gaseous reservoir grows, we numerically solve the radial diffusion equation (Lynden-Bell & Pringle 1974; Pringle 1981)

$$\frac{\partial \Sigma_g}{\partial t} = 3a^{-1} \frac{\partial}{\partial a} \left(a^{1/2} \frac{\partial}{\partial a} \{ \nu \Sigma_g a^{1/2} \} \right) + \left(\frac{\partial \Sigma_g}{\partial t} \right)_v \quad (1)$$

for the evolution of the surface density (see also Bromley & Kenyon 2011a). Here, a is the radial distance from the central star, ν is the viscosity, and t is the time. The first term is the change in Σ_g from viscous evolution; the second term is the change in Σ_g from vaporization of small solid particles.

To set the viscosity in each annulus, we adopt a standard prescription

$$\nu = \alpha c_s H_g, \quad (2)$$

where α is the dimensionless viscosity parameter, c_s is the sound speed, and H_g is the vertical scale height of the gas. Following Metzger et al. (2012), we set $\alpha = 10^{-3}$. For disk material

with angular velocity $\Omega = (GM_\star/a_0^3)^{1/2}$, $H_g = c_s\Omega^{-1}$. The sound speed is

$$c_s = \left(\frac{\gamma k_B T_g}{\mu m_H} \right)^{1/2}, \quad (3)$$

where $\gamma = 5/3$ is the ratio of specific heats, k_B is the Boltzmann constant, T_g is the gas temperature, $\mu = 28$ is the mean molecular weight, and m_H is the mass of a hydrogen atom.

In this application, the energy generated from viscous mass transport is negligible. To avoid solving for the physical conditions in the gas (e.g., Melis et al. 2010), we adopt a simple expression for the gas temperature

$$T_g = T_0 \left(\frac{a}{R_\odot} \right)^{-n}, \quad (4)$$

with $T_0 \approx 1500$ K and $n = 1/2$. This expression is similar to the more detailed results of Melis et al. (2010), where $T_0 \approx 1500$ – 3000 K and $n = 0.25$ – 0.75 for white dwarfs with effective temperatures $T_{eff} = 5000$ – 15000 K. To quantify the impact of the adopted T_0 , we also consider evolution of the gas for $T_0 = 3000$ K.

To solve eq. 1 with input α and T_g , we specify an inner radius $a_1 = 1.5 R_\star$ and an outer radius $a_2 = 1$ AU. The large outer radius allows vaporized solids to expand well past the Roche limit. Setting $x = 2a^{1/2}$, we divide the disk into 1001 annuli equally spaced in x (see also Bath & Pringle 1981, 1982). As a standard boundary condition, $\Sigma(a_1) = \Sigma(a_2) = 0$. Within every coagulation time step, our explicit algorithm for the radial surface density executes a set of n internal time steps to satisfy the Courant condition and to enable mass conservation to machine accuracy. As a check, we also derive an implicit solution for $\Sigma_g(t)$ (Press et al. 1992). Over the full range in a , the two solutions yield the same Σ_g to better than 0.1% over 1–10 Myr of evolution.

At the start of each calculation, the vertical scale height of solids is much larger than the vertical scale height of the gas. For the solids, $H \approx \nu a \approx 7500$ km at $a \approx 1.15 R_\odot$. The gas has a vertical scale height $H_g \approx c_s\Omega^{-1} \approx 1500$ km. One of our goals is to learn whether collisional processes lead to situations with $H \lesssim H_g$.

3. RESULTS

To explore the evolution of a gaseous disk generated by the vaporization of small solids, we first consider collisional cascade simulations with $r_0 = 1$ km and $\dot{M}_0 = 10^7 - 10^{13}$ g s⁻¹. The range for \dot{M}_0 includes accretion rates inferred for metallic line white dwarfs (Wyatt

et al. 2014; Farihi 2016). Calculations with $r_0 = 1$ km minimize shot noise, which grows with increasing r_0 (KB2017).

Fig. 1 (lower panel) illustrates the evolution of the total mass in solids, M_d , for various \dot{M}_0 listed in the caption. At the start of each calculation, the annulus contains no mass. As mass is added, the collision rate is negligible. Thus, M_d increases linearly with time. Once the mass reaches a critical limit, destructive collisions among the solids begin to produce smaller objects. In turn, collisions between the larger and smaller objects generate even more debris. This process fuels a collisional cascade which grinds large objects into small dust grains. After many collision times, the rate the cascade processes mass equals the input rate \dot{M}_0 . The mass in solids then achieves a roughly stable value which is maintained for the rest of the calculation. In systems with large (small) \dot{M}_0 , this mass varies slightly (noticeably) with time.

Fig. 1 (upper panel) follows the evolution of the vaporization rate \dot{M}_v . At the start of the calculation, collisions among large objects are rare; \dot{M}_v is close to zero. Once the collisional cascade begins, \dot{M}_v rises abruptly and then finds a plateau level where $\dot{M}_v = \dot{M}_0$. For systems with smaller \dot{M}_0 , there are modest variations in \dot{M}_v about the input rate \dot{M}_0 .

Fig. 2 plots results for calculations with $r_0 = 100$ km. When r_0 is large, the shot noise in the input rate is also large. The mass of solids in the annulus then grows episodically with time (Fig. 2, lower panel). Once the annulus contains several large objects, the collisional cascade begins. When \dot{M}_0 is large, the cascade processes mass at roughly the same rate as the input rate \dot{M}_0 . The mass in the annulus then exhibits small oscillations about an equilibrium mass which is somewhat larger than the equilibrium mass for smaller r_0 (KB2017).

For any \dot{M}_0 , the number of large objects required to initiate the cascade is $N_{min} \gtrsim 2$. Systems with smaller \dot{M}_0 then take longer to start a cascade. Once the cascade begins, collisions convert large objects into small objects at a rate that depends only on the mass in the annulus. This rate is independent of \dot{M}_0 . For systems with smaller \dot{M}_0 , collisions process mass at rates much larger than the input rate. The system then oscillates between high states where the collisional cascade processes mass rapidly and low states where the system slowly gains enough mass to begin a new cascade.

The oscillations in M_d produce similar variations in \dot{M}_v (Fig. 2). Throughout the evolution, \dot{M}_v is dominated by shot noise from occasional collisions among the largest objects. When \dot{M}_0 is large, there are always enough large objects to produce a continuous cascade; \dot{M}_v then varies slowly about an equilibrium rate comparable with \dot{M}_0 . When \dot{M}_0 is small, the cascade is intermittent. During the high state, \dot{M}_v achieves the equilibrium level of systems with large \dot{M}_0 . As the system falls into the low state, \dot{M}_v drops to zero.

Systems with different starting values for r_0 and \dot{M}_0 behave similarly (KB2017). When r_0 is small and \dot{M}_0 is large, the evolution of the system is very smooth. The cascade then always adjusts to balance the collision rate with \dot{M}_0 ; $\dot{M}_v = \dot{M}_0$. When r_0 is large and \dot{M}_0 is small, the evolution is oscillatory. In these systems, the cascade cannot find an equilibrium where the rate mass flows down the mass distribution (from large objects to small objects) and the vaporization rate \dot{M}_v equal the mass input rate \dot{M}_0 . Instead, the annulus gradually collects solid material over long time scales when the collisional cascade is dormant and \dot{M}_v is negligible. Once there is enough material to collide, episodic cascades generate a large \dot{M}_v which is much larger than \dot{M}_0 .

From a large suite of calculations with $r_0 = 0.1\text{--}10$ km, $\dot{M}_0 = 10^5 - 10^{13}$ g s⁻¹, and $a = 0.5\text{--}3 R_\odot$ (KB2017), the solid mass in the equilibrium state is

$$M_{d,eq} \approx 1.5 \times 10^{19} \text{ g} \left(\frac{\dot{M}}{10^{10} \text{ g s}^{-1}} \right)^{1/2} \left(\frac{0.6 M_\odot}{M_{wd}} \right)^{9/20} \left(\frac{r_0}{1 \text{ km}} \right)^{1.04} \left(\frac{\rho_s}{3 \text{ g cm}^{-3}} \right)^{9/10} \left(\frac{0.01}{e} \right)^{4/5} \left(\frac{\Delta a}{0.2a} \right)^{1/2} \left(\frac{a_0}{R_\odot} \right)^{43/20} \quad r_0 \gtrsim 1 \text{ km} . \quad (5)$$

Aside from the numerical coefficient, the dependence of the equilibrium mass in solids on the seven physical variables in eq. 5 is a consequence of simple collision theory (KB2017). When a system has episodic cascades, the maximum mass is close to the equilibrium mass for large \dot{M}_0 (KB2017).

The expression for $M_{d,eq}$ in eq. 5 helps us establish approximate conditions for episodic collisional cascades. In any swarm of solids, the minimum mass in solids required for a cascade is $M_{d,min} \approx N_{min} m_0$ with $N_{min} \approx 2$. When $M_{d,min} \geq M_{d,eq}$, the system cannot find an equilibrium and oscillates between the high and low states. Fixing all variables except a_0 , \dot{M}_0 , and r_0 in eq. 5 at their nominal values, setting $N_{min} = 2$ leads to a simple estimate for the maximum \dot{M}_0 in the episodic regime:

$$\dot{M}_{max,ch} \lesssim 3 \times 10^4 \text{ g s}^{-1} \left(\frac{r_0}{1 \text{ km}} \right)^{3.92} \left(\frac{a_0}{R_\odot} \right)^{-86/20} . \quad (6)$$

Systems with $\dot{M}_0 \gtrsim \dot{M}_{max,ch}$ ($\lesssim \dot{M}_{max,ch}$) always (never) achieve a steady-state with the equilibrium mass in eq. 5. For our annulus with $a_0 = 1.16 R_\odot$, the maximum \dot{M}_0 required for the episodic regime ranges from 3×10^4 g s⁻¹ for $r_0 = 1$ km to 8×10^7 g s⁻¹ for $r_0 = 10$ km to 7×10^{11} g s⁻¹ for $r_0 = 100$ km. The full suite of simulations confirms this general result.

The two types of collisional cascades generate different evolutionary sequences for gaseous disks orbiting the central white dwarf. To illustrate this behavior, we again begin with a

discussion of simulations with $r_0 = 1$ km and various \dot{M}_0 . In these calculations, the smooth time evolution of \dot{M}_v leads to a fairly calm gaseous disk with a constant accretion rate onto the white dwarf.

Fig. 3 illustrates several snapshots of the gas surface density for a system with $r_0 = 1$ km and $\dot{M}_0 = 10^{13}$ g s $^{-1}$. Initially, the disk contains no gas; $\Sigma_g = 0$ for all a . When the cascade begins at $t = 8$ yr (pink curve), vaporized solids generate a narrow torus of gas at $a \approx 1.15 R_\odot$. As vaporization continues to place gas in this annulus, viscosity spreads the gas to smaller and to larger radii (see also Lynden-Bell & Pringle 1974). After a few hundred years (lime curve), the gas begins to accrete onto the central star. Over the next few hundred years, the surface density of gas near the white dwarf photosphere grows to rival the surface density of gas at the Roche limit (dark green and blue curves). By $t = 3000$ – 7000 yr, the gaseous disk has evolved into a structure where the surface density falls monotonically from 2–3 stellar radii to 10–30 times the Roche limit. As the evolution continues, the inner disk maintains a roughly static structure. Beyond the Roche limit, however, the outer disk radius continues to expand.

Fig. 4 plots the evolution of \dot{M}_\star , the mass accretion rate of gas from the disk onto the white dwarf for this model (dark magenta curve) and other models with $r_0 = 1$ km and smaller \dot{M}_0 (as listed in the legend). At early times, the collisional cascade is dormant. Once the cascade begins, vaporized solids generate a thin annulus of gas. Eventually, viscous evolution transports the gas from the Roche limit onto the white dwarf. The derived \dot{M}_\star then grows dramatically, rising from 1–10 g s $^{-1}$ to a rate approaching \dot{M}_0 in a few thousand years. After 10^4 – 10^5 yr, \dot{M}_\star reaches a plateau. In systems with large \dot{M}_0 ($\gtrsim 10^9$ g s $^{-1}$), $\dot{M}_\star \approx 0.9\dot{M}_0$. When \dot{M}_0 is smaller ($\lesssim 10^9$ g s $^{-1}$), \dot{M}_\star oscillates about this equilibrium rate.

For any \dot{M}_0 , the time scale to reach the plateau phase depends on the viscosity. In our calculations, the viscosity is sensitive to α and to the gas temperature T_g (eq. 2). Systems with factor of ten smaller (larger) α reach the plateau phase ten times more slowly (rapidly). Similarly, raising (lowering) T_g by a factor of two decreases (increases) the viscous time by a factor of two.

Although the time scale to reach the plateau phase depends on α and T_g , the plateau \dot{M}_\star is insensitive to either variable. In all of our calculations with $r_0 = 1$ km, the plateau rate is always roughly 90% of the input \dot{M}_0 .

Based on a broad suite of simulations with $r_0 = 0.1$ – 10 km and a variety of \dot{M}_0 , the mass in the disk is independent of r_0 , ρ_s , and other properties of the solids. In addition to

\dot{M}_0 , the mass in gas depends on α and T_g :

$$M_g \approx 2.2 - 2.4 \times 10^{22} \text{ g} \left(\frac{\dot{M}}{10^{10} \text{ g s}^{-1}} \right) \left(\frac{1500 \text{ K}}{T_0} \right) \left(\frac{10^{-3}}{\alpha} \right). \quad (7)$$

Comparing this numerical result with eq. 5, the equilibrium mass in the gaseous disk is roughly three orders of magnitude larger than the equilibrium mass in solids.

In calculations with larger r_0 , the structure of the disk and the rate of mass accretion onto the white dwarf oscillate between low and high states. Fig. 5 shows the evolution for five simulations with $r_0 = 100 \text{ km}$ and $\dot{M}_0 = 10^9 - 10^{13} \text{ g s}^{-1}$. When \dot{M}_0 is large, the evolution is smooth. The mass accretion rate onto the white dwarf gradually increases to the plateau value in $10^4 - 10^5 \text{ yr}$. As the input \dot{M}_0 drops, high \dot{M}_* states becomes more and more episodic. On time scales of 0.1–1 Myr, the variations in \dot{M}_* grow from $\pm 5\%$ at $\dot{M}_0 = 10^{12} \text{ g s}^{-1}$ to $\pm 50\%$ at $\dot{M}_0 = 10^{11} \text{ g s}^{-1}$ to ± 2 orders of magnitude at $\dot{M}_0 = 10^{10} \text{ g s}^{-1}$ to $\pm 6-8$ orders of magnitude at $\dot{M}_0 = 10^9 \text{ g s}^{-1}$.

Although the time scale for changes in \dot{M}_* depends on α and T_g , the overall fluctuations are sensitive only to r_0 and \dot{M}_0 . When r_0 is large and \dot{M}_0 is small, \dot{M}_* varies by many orders of magnitude over 0.1–1 Myr time scales. Smaller r_0 and larger \dot{M}_0 smooth out the variations in \dot{M}_* .

For calculations with $r_0 = 30-100 \text{ km}$ and $\dot{M}_0 \gtrsim 10^{12} \text{ g s}^{-1}$, the typical mass in the disk is close to the equilibrium mass in eq. 7. Due to stochastic variations in \dot{M}_v , the mass varies by $\pm 10\%-20\%$ about the equilibrium mass. Smaller \dot{M}_0 leads to large oscillations in \dot{M}_v and similarly large variations in M_g . When the collisional cascade generates large \dot{M}_v , the *maximum* disk mass is roughly 10^{23} g for $T_0 = 1500 \text{ K}$ and $\alpha = 10^{-3}$. This maximum mass scales with α and T_0 as in eq. 7. During low states, $M_g \lesssim 10^{10} \text{ g}$. Throughout a single oscillation, the total variation in M_g is more than fifteen orders of magnitude.

For all systems, the fraction of time in the high state is a strong function of r_0 and \dot{M}_0 (KB2017). In principle, the variation of the mass in gas provides a reasonable proxy for the time spent in high and low states. However, detecting the gas depends on the thermodynamic state of the disk and the ability of spectrographs to distinguish absorption or emission lines produced in the disk from those generated in the white dwarf photosphere. The X-ray luminosity probably enables a clearer picture. Despite uncertainties in the likely X-ray temperature, the X-ray luminosity provides an instantaneous measure of the accretion rate from the disk onto the white dwarf (e.g., Kuulkers et al. 2006; Pretorius & Knigge 2012; Reis et al. 2013, and references therein).

To predict the X-ray luminosity, we assume that half of the accretion energy is radiated in a boundary layer between the disk and the white dwarf (e.g., Lynden-Bell & Pringle 1974)

or at the base of a magnetic accretion column (e.g., Ghosh & Lamb 1979). Ignoring factors of order unity, $L_X \approx GM_* \dot{M}_* / 2R_*$. The fraction of time with $L_X/L_\odot \gtrsim 10^{-n}$ with integer n follows directly from our calculations.

Fig. 6 plots our results. In the lower panel, the solid curve indicates the X-ray luminosity as a function of the accretion rate onto the white dwarf, $L_X \approx 5 \times 10^{16} \dot{M}_*$ erg s⁻¹. When the mass input rate for solids is large, $\dot{M}_0 \gtrsim \dot{M}_{0,crit} \approx 3 \times 10^4 (r_0/1 \text{ km})^{3.92}$ g s⁻¹, the collisional cascade steadily feeds the gaseous disk. Accretion onto the white dwarf is also steady. When \dot{M}_0 falls below $\dot{M}_{0,crit}$, the X-ray luminosity varies between low states with $L_X \approx 0$ and $L_X \approx L_{X,crit} \approx 5 \times 10^{16} \dot{M}_{0,crit}$ erg s⁻¹. The vertical dashed lines in the lower panel indicate the critical \dot{M}_0 for values of r_0 listed in the legend.

The upper panel in Fig. 6 shows predictions for the fraction of time a system spends with $L_X/L_\odot \gtrsim 10^{-7}$. For systems with $r_0 \lesssim 10$ km, \dot{M}_* and the X-ray luminosity are nearly constant in time. The white dwarf is above the reference luminosity all of the time or none of the time. When r_0 is larger, episodic evolution of \dot{M}_* leads to a broad range of X-ray luminosities for any combination of r_0 and \dot{M}_0 . In our calculations, swarms with $r_0 = 30$ km are detectable X-ray sources at least some of the time. The windows for detecting swarms with $r_0 \gtrsim 100$ km are much smaller.

As an illustration of the utility of Fig. 6, we consider two examples. For a system with $r_0 = 10$ km, the critical accretion rate and X-ray luminosity are $\dot{M}_{0,crit} \approx 2.5 \times 10^8$ g s⁻¹ and $L_{X,crit} \approx 10^{25}$ erg s⁻¹. When $\dot{M}_0 \gtrsim 2.5 \times 10^8$ g s⁻¹, we expect an accretion luminosity along the diagonal solid curve in the lower panel. For smaller accretion rates, the system has L_X between zero and $L_{X,crit}$. This critical L_X is smaller than $10^{-7} L_\odot$. Thus, the fraction of time with $L_X/L_\odot > 10^{-7}$ is zero.

For a second example, suppose a metallic line white dwarf has $L_X \approx 10^{-7} L_\odot$. The implied accretion rate is 7.6×10^9 g s⁻¹. In the lower panel, this rate is larger than (smaller than) critical rates for $r_0 = 1\text{--}20$ km (25–100 km). Thus, this system could have a steady-state collisional cascade with $r_0 \lesssim 10$ km or an intermittent cascade with $r_0 \gtrsim 25$ km. Moving to the upper panel, the fraction of time systems with $r_0 = 1\text{--}10$ km spend in this high L_X state is either unity (if $\dot{M}_0 \gtrsim 7.6 \times 10^9$ g s⁻¹) or zero (if $\dot{M}_0 \lesssim 7.6 \times 10^9$ g s⁻¹). Systems with $r_0 = 30$ km (100 km) spend all of their time at or above this L_X when $\dot{M}_0 \gtrsim 2 \times 10^{10}$ g s⁻¹ ($\dot{M}_0 \gtrsim 2 \times 10^{12}$ g s⁻¹). Otherwise, the fraction of time spent at this L_X is roughly $\dot{M}_0/\dot{M}_{0,crit}$.

In these examples, a single L_X observation places few constraints on the model. Surveys with at least 10–20 detections or upper limits begin to carve out allowed sections of (r_0, \dot{M}_0) space. Combined with estimates of accretion rates derived from photospheric abundance

measurements, these data begin to test the model.

4. DISCUSSION

4.1. Simple Physical Model for Metallic Line White Dwarfs

In KB2017 and this paper, we have described a simple physical model for the delivery of metals to a white dwarf photosphere. In this model, at least one mechanism places large asteroids with radius r_0 and mildly eccentric orbits into a ring near the Roche limit of a white dwarf at a constant rate \dot{M}_0 . Interactions among the solids generate a collisional cascade, which produces swarms of $1 \mu\text{m}$ dust grains. Vaporization of the grains feeds a ring of gas. Viscous processes spread the ring into a disk; material from the disk accretes onto the central white dwarf.

The main parameters in this picture are r_0 and \dot{M}_0 . When $\dot{M}_0 \gtrsim \dot{M}_{0,crit} \approx 3 \times 10^4 (r_0/1 \text{ km})^{3.92} \text{ g s}^{-1}$, the solids find an equilibrium state where (i) \dot{M}_v , the vaporization rate of the grains, roughly equals \dot{M}_0 and (ii) the mass of the gaseous disk and the X-ray luminosity are roughly constant in time. Small solids with $r_0 \lesssim 1 \text{ km}$ find equilibrium with relatively small \dot{M}_0 . Larger solids with $r_0 = 10 \text{ km}$ (100 km) require input rates $\dot{M}_0 \gtrsim 2.5 \times 10^8 \text{ g s}^{-1}$ ($\dot{M}_0 \gtrsim 2 \times 10^{12} \text{ g s}^{-1}$). Once the system achieves equilibrium, metals accrete onto the white dwarf at a rate $\dot{M}_\star \approx 0.9 \dot{M}_0$. Although most of the vaporized metals accrete onto the white dwarf, viscosity spreads some of the mass to large distances from the central star.

When $\dot{M}_0 \lesssim \dot{M}_{0,crit}$, the time for the ring to accumulate enough solids for a collisional cascade is longer than the time scale for the cascade to deplete the ring of solids. In these circumstances, the system oscillates between low states (where the mass in solids slowly grows with time, $\dot{M}_v \ll \dot{M}_0$, and the X-ray luminosity is negligible) and high states (where the mass rapidly declines with time, $\dot{M}_v \gg \dot{M}_0$, and the X-ray luminosity is substantial). As long as the viscous time scale is shorter than the cycle time between high and low states, the mass accretion rate onto the white dwarf varies by orders of magnitude on time scales of thousands to millions of years.

In a more realistic system where \dot{M}_0 and r_0 vary on short time scales, the behavior of the solids and the gaseous disk depends on the variability time scale. When the cascade is active, the collision time for the largest objects ranges from the orbital period (for large \dot{M}_0) to a few months (for small \dot{M}_0). On this time scale, the cascade adjusts the vaporization rate and the production rate of small particles to match the time-variable \dot{M}_0 and r_0 . In this way, changes in \dot{M}_0 and r_0 can generate substantial variations in the IR excess from $1 \mu\text{m}$

particles and the amount of gas near the Roche limit on week or longer time scales.

When $\alpha \approx 10^{-3}$, the viscous time is roughly $10^4 - 10^5$ orbital periods, ~ 10 yr. In an active cascade, variations in \dot{M}_0 and r_0 for the solids produce similar scale fluctuations in \dot{M}_* . Although variability in L_X correlates with changes to the IR excess and the amount of gas near the Roche limit, there is a 10 yr or longer delay between rises/drops in L_X and the IR excess. This delay is roughly proportional to α . When the cascade is not active, \dot{M}_v and \dot{M}_* are close to zero. Substantial variations in \dot{M}_0 and r_0 are invisible.

In any of the examples we studied, the vertical scale height of the solids remains large. If solids have $e_0 = 0.01$ and inclination $i_0 = e_0/2$, the cascade removes solids faster than collisional damping can reduce the vertical scale height (KB2017). Thus, the solids do not evolve into the optically thick, vertically thin structure originally suggested by Jura (2003).

4.2. Comparisons with Previous Results

Although our approach is the first to combine collisional evolution of solids with viscous diffusion of gas, other investigators have treated aspects of these phenomena in the context of metallic line white dwarfs. In this sub-section, we compare the methodologies and results of these studies with our own.

Brown et al. (2017) consider the tidal destruction, sublimation, and ultimate fate of rocky and icy asteroids with periastron distances $q \approx R_*$. In this situation, large solids tidally fragment; small solids are tidally stable but sublimate. Delivery of material onto the white dwarf then depends on the initial radius, composition, and q for each asteroid. In a manner similar to meteors encountering the Earth, larger fragments ablate in the white dwarf atmosphere; icy fragments ablate more rapidly than rocky ones. Smaller fragments often sublimate before reaching the atmosphere; the resulting gas then rains down onto the white dwarf. With no calculation for the long-term evolution of gas, estimates for \dot{M}_* rely on the rate of direct collisions of asteroid with the white dwarf or assumptions on the subsequent evolution of gas orbiting the white dwarf.

Our somewhat different analysis of tidal forces (KB2017) indicates that solids with $r_0 \lesssim 100$ km and $\rho_s = 3$ g cm $^{-3}$ are stable at distances $a \gtrsim 0.7a_R$, where a_R is the distance of the Roche limit from the center of the white dwarf (see also Veras et al. 2017). Our calculations do not address the fate of solids at smaller a . Although our conclusions on the sublimation of large particles are similar to Brown et al. (2017), the sublimation time for particles with radii $r \gtrsim 1$ μ m is longer than the collision time throughout the collisional cascade. Thus, it is reasonable for us to neglect sublimation for large particles and focus on the sublimation

of the smallest particles that feed the gaseous disk. Compared to Brown et al. (2017), our estimates for \dot{M}_\star rely on viscous diffusion through a gaseous disk instead of direct collision with the white dwarf.

In their investigation of the evolution of disks containing cm-sized solids interacting with a viscous, gaseous disk, Metzger et al. (2012) solve a radial diffusion equation similar to our eq. 1 (see also Rafikov 2011a,b; Bochkarev & Rafikov 2011; Rafikov & Garmilla 2012). Adopting a very small vertical scale height for the solids, they treat the back-reaction of the solids on the gas; in our treatment, the much larger vertical scale height of the solids implies a negligible back-reaction which is safely ignored. While we adopt a constant α and allow the disk temperature to vary with distance from the central star, Metzger et al. (2012) adopt a constant disk temperature and let α vary with radius. For a similar $\Sigma(a)$, the magnitude and variation of $\nu(a)$ – which controls the evolution of the surface density of the gas – is similar in the two approaches. The time scale for a ring of gas to accrete onto the star from some distance a is also similar.

Adopting a fixed initial mass for the solids, M_d , Metzger et al. (2012) derive \dot{M}_\star as a function of M_d and other properties of the solids and the gas. When the solids are optically thin (thick), \dot{M}_\star is roughly 100 times smaller (larger) than the rate generated by PR drag, $\dot{M}_\star \approx 10^{-8} \text{ g s}^{-1}$. Interactions between opaque disks of solids and gas can also generate large time-variations in \dot{M}_\star . In contrast, the \dot{M}_\star derived in our calculation depends on an adopted input rate \dot{M}_0 and typical radius r_0 for solids near the Roche limit; oscillations in \dot{M}_\star occur when \dot{M}_0 is small and r_0 is large.

Bear & Soker (2013) combine an analysis of tidal disruption (similar to Brown et al. 2017) with a simple treatment for viscous disk evolution (compared to Metzger et al. 2012) to propose that infalling asteroids drive transient accretion events similar to those associated with supermassive black holes at the centers of galaxies (e.g., Rees 1988; Cannizzo et al. 1990; Gezari et al. 2009; Lodato & Rossi 2011; Bromley et al. 2012; Kochanek 2016, and references therein). Assuming that (i) a massive ($\gtrsim 10^{20} \text{ g}$) asteroid is completely converted into gas by collisions and sublimation, (ii) the gas has a high temperature derived from the kinetic energy of infall, and (iii) the gas lies in a vertically thin, optically thick disk, they infer a peak accretion rate exceeding 10^{13} g s^{-1} and X-ray luminosity exceeding $10^{30} \text{ erg s}^{-1}$ over a typical lifetime of a few days to a few weeks.

In our approach, the collision velocities of asteroid fragments on $e \approx 1$ orbits are set by the velocity dispersion of the fragments, not their orbital velocity. Numerical simulations suggest tidal disruption of asteroids generates a long string of fragments along an orbit with similar e and i as the original asteroid (e.g., Debes et al. 2012b). Unless other processes change e and i , we expect low velocity collisions among the fragments to produce a cascade

similar to those calculated here. With most interactions near periastron of a large e orbit, modest vaporization results in gas ejected from the orbit. Subsequent evolution of the gas depends on the collision frequency, the vaporization of small particles, and the temperature and viscosity of the gas. Detailed numerical simulations are necessary to learn the fate of this material; we speculate that the white dwarf accretes gas with a typical temperature of 10^4 – 10^5 K at some modest background rate set by continuous vaporization of small particles, with occasional flares from the production of debris from collisions of larger fragments.

To constrain the frequency and sizes of accreted asteroids among metallic line white dwarfs, Wyatt et al. (2014) explore analytical estimates and Monte Carlo calculations which consider how derived accretion rates depend on the gravitational settling time in the white dwarf atmosphere, the distributions of accretion rates and masses for accreted asteroids, and the typical time scale for vaporized solids to accrete onto the white dwarf. Their results suggest that white dwarfs accrete solids ranging in size from $\lesssim 1$ –10 km to 100–1000 km at rates ranging from $\sim 10^6$ g s $^{-1}$ to $\sim 10^{11}$ g s $^{-1}$ with a median of 10^{-8} g s $^{-1}$. Smaller solids are much more common than larger solids. In DA white dwarfs with short settling times, accretion of 1–30 km objects is nearly continuous. Asteroids with radii of 30–100 km dominate the pollution of non-DA white dwarfs with much longer settling times. The time scale for a gaseous disk to deposit metals onto the white dwarf photosphere is 20–1000 yr.

Our calculations are consistent with these results. Disk time scales of 20–1000 yr imply $\alpha = 0.05$ – 10^{-3} , close to the range deduced in the accreting white dwarfs of cataclysmic variables (e.g., Smak 1999; King et al. 2007; Kotko & Lasota 2012). For the range of accretion rates derived in Wyatt et al. (2014), our analysis suggests continuous accretion for $r_0 = 1$ –10 km and episodic accretion for $r_0 \gtrsim 30$ km. The division between episodic and continuous accretion agrees rather well with the expectations for DA and non-DA white dwarfs from Wyatt et al. (2014).

Overall, these and other analyses paint a fairly coherent picture for the transport of metals from a region near the Roche limit onto the surface of a white dwarf. In some fashion, dynamical processes regularly transport material from large a to the Roche limit of the white dwarf (Wyatt et al. 2014). Well inside the Roche limit, tidal forces disrupt the solids into fragments (e.g., Holsapple & Michel 2006, 2008; Debes et al. 2012b; Bear & Soker 2013; Veras et al. 2014a, 2017; Brown et al. 2017). If large solids or disrupted fragments begin to collide, they are rapidly ground into small dust grains (KB2017, this paper). UV radiation from the white dwarf rapidly sublimates small solids and slowly evaporates larger objects (this paper; see also Veras et al. 2015a; Brown et al. 2017). Viscous processes transport vaporized solids to the central star (this paper; see also Metzger et al. 2012; Bear & Soker 2013).

Despite the attractiveness of this picture, there are many uncertainties. Plausible mechanisms for delivering solids to the Roche limit have few observational constraints (e.g., Debes et al. 2012b; Frewen & Hansen 2014; Veras et al. 2015b; Payne et al. 2016; Hamers & Portegies Zwart 2016; Antoniadou & Veras 2016; Brown et al. 2017). Models for disk evolution are rather simple, with limited treatment of interactions between the solids and the gas. Aside from explaining the transport of solids to the white dwarf, it is not yet clear whether the model can account for other aspects of observations. In the next few sub-sections, we comment on these issues in more detail.

4.3. Delivery of Solids to the Roche Limit

Various groups have considered the delivery of solid objects to a volume within the Roche limit of a white dwarf (e.g., Debes & Sigurdsson 2002; Veras et al. 2014b; Veras & Gänsicke 2015; Bonsor & Veras 2015; Antoniadou & Veras 2016; Veras 2016; Payne et al. 2017; Brown et al. 2017; Petrovich & Muñoz 2017; Stephan et al. 2017; Caiazzo & Heyl 2017). All models begin with a main sequence star and a surrounding planetary system. While on the main sequence, the nearly constant luminosity of the central star establishes the ‘snow line’, which marks the boundary between an inner ‘terrestrial’ region with little volatile material and an outer ‘icy’ region where volatiles can condense from the gas phase onto solids (e.g., Kennedy & Kenyon 2008). As the central star evolves into a red giant and then an asymptotic branch giant, the increasing luminosity of the central star moves the snow line outward and bakes solids between the ‘original’ and ‘new’ snow lines (Stern et al. 1990; Parriott & Alcock 1998; Villaver & Livio 2007; Dong et al. 2010; Bonsor et al. 2011; Veras et al. 2013; Mustill et al. 2014; Malamud & Perets 2016, 2017a,b). The slowly decreasing mass of the central star also results in an expansion and possible destabilization of orbiting solids. If destabilization is sufficiently traumatic, solids can attain extremely eccentric orbits with periastra inside the Roche limit of the white dwarf central star. After some number of passes close to the white dwarf, tidal forces disrupt the solids into much smaller objects.

In addition to a lack of agreement on the mechanism(s) that place(s) solids on very eccentric orbits, it is unclear how the orbits of small solids objects evolve from $e = 0.99$ to $e \lesssim 0.1$. Although we do not address this issue directly, our calculations provide some constraints on likely outcomes of plausible paths from high e to small e orbits. In mechanisms where long-term dynamical processes such as PR drag gradually circularize the orbits (e.g., Veras et al. 2014a), the long-term outcome is probably similar to that outlined here (see also KB2017): once the orbits of the solids cross, a collisional cascade generates small objects

which vaporize and feed a gaseous disk. Although the geometry and observable properties of the cascading solids and the disk depend on the mass and orbital properties of the incoming solids, outcomes are probably similar to those outlined here.

If long-term dynamical solutions are unreliable, our results indicate that collisions are insufficient to reduce e and i dramatically on their own. Some other mechanism is required. If two asteroids with large e collide inside the Roche limit, they probably vaporize. The gas released from this collision might be sufficient to reduce e for other asteroids following similar paths around the white dwarf. Interactions between incoming asteroids with the magnetic field of the white dwarf may generate sufficient electromagnetic induction and Ohmic dissipation to reduce e on time scales ranging from a few Myr to several Gyr (Bromley & Kenyon, in preparation; see also Li et al. 1998).

Incorporating any mechanism for the delivery of solids to the Roche limit into our calculations requires more comprehensive theoretical predictions of outcomes for the evolution of gas and solids as the central star begins to evolve into a white dwarf. For example, detailed predictions for the distributions of Σ , a , e , and i for swarms of solids outside the Roche limit would allow us to learn how outcomes for the delivery of solids to the white dwarf depend on the delivery mechanism.

4.4. Improved Models for Evolution of the Gas

In this first exploration of the evolution of a gaseous disk fed by a collisional cascade, we assume the gas is axisymmetric and adopt a simple prescription for the disk temperature (see also Jura 2008; Melis et al. 2010). Although our approach is reasonable, we outline several possible improvements for future studies.

By analogy with the circumstellar disks in cataclysmic variables (Meyer & Meyer-Hofmeister 1982; Mineshige & Osaki 1983; Cannizzo & Wheeler 1984) and pre-main sequence stars (D’Alessio et al. 1998; Najita et al. 2011, 2013), we expect a complex temperature structure for gas fed by a collisional cascade. For optically thin disks where the solids have negligible vertical scale height ($H \ll H_g$), Melis et al. (2010) derived the radial temperature structure outside $25 R_\star$ for an ionized gas with Mg, Si, Ca, and Fe. However, our disks have $H > H_g$; an improved calculation should include interactions between the gas and dust. As one example, combining the formalism of Najita et al. (2013) with our derived radial surface density distribution should enable calculations of the radial and vertical temperature structure from the inner edge of the disk out past the Roche limit. Since the evolution of Σ depends on T_g , a better prescription for T_g would yield a better connection between the

input (r_0, \dot{M}_0) and the output \dot{M}_* and L_X .

Our solution of the radial diffusion equation assumes the white dwarf has a negligible magnetic field. When the field has a modest strength, it can truncate the disk and channel gas directly onto the white dwarf photosphere (e.g., Ghosh & Lamb 1979; Metzger et al. 2012; Mukai 2017, and references therein). In some configurations, the field might be able to trap dust and gas in the magnetosphere (e.g., Farihi et al. 2017a). If most metallic line white dwarfs have modest to large magnetic fields, it will be necessary to address whether the field has any impact on small particles in the collisional cascade.

Eventually, it should be possible to relax the assumption of an axisymmetric disk. Our calculations assume that vaporization places material uniformly within an annulus. In a real system, vapor generated from collisions of 1 km and larger solids is clumpy. Naively, we expect more clumpiness from collisions of larger objects. The azimuthal structure of the disk then depends on the viscous time scale relative to the time scale for collisions of the largest objects. When the viscous time scale is shorter than the collision time, viscosity rapidly spreads out blobs of gas; the disk is more axisymmetric. When the collision time is shorter than the viscous time, small particles are vaporized faster than viscous shear can spread the gas. The disk is then more asymmetric.

4.5. Gas Drag

Although we have not included interactions between the solids and gas in our simulations, it is straightforward to show that the gas has little impact on collisional cascades with $e_0 = 0.01$. In protoplanetary and circumplanetary disks, massive solid objects modify the density structure of the gas (e.g., Ward 1997; Tanaka et al. 2002; Masset & Papaloizou 2003; Nelson & Papaloizou 2004; Ida & Lin 2008; Lyra et al. 2010; Bromley & Kenyon 2011b, 2013, and references therein); gravitational torques generated by these structures induce radial migration of the solids. For gaseous disks inside the Roche limit, the time scale for migration is rarely shorter than the viscous time but is much shorter than the cooling time for the white dwarf. Thus, stable solids *could* migrate on interesting time scales. However, these time scales are much longer than the collision time. In the context of our calculations, migration is safely ignored.

In any disk with finite pressure, the gas orbits the central star somewhat more slowly than solids following Keplerian orbits (e.g., Adachi et al. 1976; Weidenschilling 1977; Youdin & Chiang 2004; Youdin 2010; Youdin & Kenyon 2013, and references therein). The solids then feel a headwind, $\Delta v = v_g - v_K$, where v_g is the orbital velocity of the gas. The

response to the headwind depends on the ‘stopping time’ t_s required for an orbiting particle to encounter its mass in gas. When the stopping time is much longer than the orbital period, T , solids do not respond to the gas. Solids with $t_s \ll T$ are entrained in the gas and drift inward or outward on the local viscous time. In between these two limits, solids drift radially inward with a maximum drift velocity Δv (Adachi et al. 1976; Weidenschilling 1977).

To derive the radial drift speed as a function of particle radius, we follow the formalism of Weidenschilling (1977) and consider drift in axisymmetric disks with a radial surface density generated by our solution to the diffusion equation, eq. 1. Given a derived $\Sigma_g(a, t)$ and an adopted γ , μ , and $T_g(a)$, we infer the gas density ρ_g and pressure P_g required to establish radial drift rates. Defining $g = v_K^2/a$ as the central gravity and $\delta g = \rho_g^{-1} \partial P_g / \partial R$ as the residual gravity, the headwind is (Weidenschilling 1977)

$$\Delta v \simeq - \left(\frac{\delta g}{2g} \right) v_k . \quad (8)$$

As a measure of the drift speed relative to the local orbital velocity, it is useful to define

$$\eta = \frac{\Delta v}{v_K} \simeq - \left(\frac{\delta g}{2g} \right) . \quad (9)$$

Weidenschilling (1977) decomposed the motion into a radial drift u and a transverse drift w , which depend on Δv and particle size. Takeuchi & Artymowicz (2001) later generalized the Weidenschilling (1977) approach to disks where Poynting-Robertson (PR) drag and radiation pressure are relevant. As in Kenyon et al. (2016), we derive u and w as a function of particle size for a system with radiation pressure but no PR drag. As discussed in KB2017, the time scale for PR drag is much longer than the collision time. Our goal is to learn whether gas drag or radiation pressure can produce radial drift of small particles on time scales shorter than the collision time. Thus, PR drag is safely ignored.

Fig. 7 illustrates results for particle drift at $a = 1.15 R_\odot$ (within the ring of solids) in a gaseous disk with the equilibrium mass, $\alpha = 10^{-3}$, no radiation pressure, and $T_0 = 1500$ K (open circles) or $T_0 = 3000$ K (open circles). The legend indicates the input \dot{M}_0 . For all systems, the maximum drift rate relative to the gas is 10–20 $R_\oplus \text{ yr}^{-1}$. With $u \propto T_g$ (Weidenschilling 1977), particles in cooler disks drift more slowly. Moving away from each maximum in the Figure, smaller particles have successively lower drift rates until they orbit with the gas. Larger particles drift more slowly because they have too much inertia for the gas to move. These particles follow Keplerian orbits.

Overall, it is clear from Fig. 7 that the radius of particles with the maximum drift velocity becomes smaller with smaller input \dot{M}_0 . Lower input rates generate disks with lower surface

density Σ_g and mass density ρ_g . During one orbit of the central star, particles see less mass in disks with smaller \dot{M}_0 than in disks with larger \dot{M}_0 . Particles in less massive disks have larger stopping times and are therefore less entrained in the gas. Thus, the maximum drift velocity moves to smaller particle size with decreasing \dot{M}_0 .

Increasing the disk viscosity parameter α has the same impact as decreasing \dot{M}_0 (Fig. 8). For disks with the same \dot{M}_0 and \dot{M}_v , those with larger α have larger viscosity, lower masses, smaller Σ_g , and larger stopping times (e.g., Lynden-Bell & Pringle 1974; Weidenschilling 1977). Compared to Fig. 7, the maximum particle velocity in disks with $\alpha = 10^{-2}$ is shifted to smaller particle sizes. Otherwise, the general variation of the drift velocity with particle size is fairly independent of α .

To derive these results, we assume that the solids and gas are well-mixed, with $H \lesssim H_g$. In our simulations, however, $H \approx 5 - 10H_g$. Because the solids travel through the gas only 10% to 20% of each orbit, the actual drift rates are 80% to 90% smaller than suggested by Figs. 7–8. Thus, the typical maximum drag rate is 2–4 $R_\oplus \text{ yr}^{-1}$.

Despite these large maximum drift velocities, the drift time is still much longer than the collision time. With a drift velocity of 2–4 $R_\oplus \text{ yr}^{-1}$, it takes more than a decade for a particle to cross our adopted ring of solids. For particles with $r = 0.3\text{--}3 \text{ cm}$ ($\dot{M}_0 = 10^{13} \text{ g s}^{-1}$), $r = 0.1\text{--}1 \text{ mm}$ ($\dot{M}_0 = 10^{11} \text{ g s}^{-1}$), or $r = 1\text{--}10 \text{ }\mu\text{m}$ ($\dot{M}_0 = 10^9 \text{ g s}^{-1}$), the collision time for a ring with the equilibrium mass in solids is $10^3 - 10^4 \text{ s}$. Thus, the collisional cascade removes small particles well before gas drag produces a significant radial drift.

In addition to producing a radial drift, the gas damps the orbital e and i of particles with $t_s \lesssim T$ (Adachi et al. 1976; Weidenschilling 1977). The damping time scale is comparable to the time scale for radial drift. With the radial drift time much longer than the collision time, the gas cannot reduce the vertical scale height of small solids before the collisional cascade grinds them to dust.

Including radiation pressure has a modest impact on this conclusion. Following Burns et al. (1979), we define the ratio of the radiation pressure to the local gravity:

$$\beta = \frac{3 Q_{pr} L_\star}{16 \pi c G r \rho_s M_\star}, \quad (10)$$

where Q_{pr} is the Mie scattering coefficient and c is the speed of light. For a $0.6 M_\odot$ white dwarf with $L_\star \approx 10^{-2} L_\odot$, $\beta \approx 0.003 (r/1 \mu\text{m})^{-1}$. With no gas in the system, small grains do not respond to radiation pressure before they are vaporized. Once small grains are entrained in the gas, however, radiation becomes more important (Takeuchi & Artymowicz 2001). With a radial drift velocity of $(\eta - \beta)t_s a \Omega^2$, grains with $\beta \gtrsim \eta$ ($\beta \lesssim \eta$) drift radially out (in) through the gas (Takeuchi & Artymowicz 2001; Kenyon et al. 2016).

For the physical conditions adopted in Figs. 7–8, small grains with $r \approx 1 \mu\text{m}$ to 1 mm drift outward at speeds of 1–100 $R_{\oplus} \text{ yr}^{-1}$. Correcting for the small fraction of time grains with large H spend interacting with the gas, it takes grains more than a year to move out of our model annulus at $1.15 R_{\odot}$. Compared to the time scale for the collisional cascade, these drift rates are still negligible.

To identify situations where gas drag *is* important, we consider the physical conditions in the solids when the time scale for radial drift is comparable to the collision time. For simplicity, we set $H \approx H_g$. From eq. 8 of KB2017, the collision time for a particle with radius r in a swarm of solids within our model annulus is

$$t_c \approx 1.6 \times 10^3 \text{ s} \left(\frac{4 \times 10^{21} \text{ g}}{M_d} \right) \left(\frac{r}{1 \text{ km}} \right), \quad (11)$$

where M_d is the total mass in solids. Setting the collision time to 1 yr yields the mass where the collision time is roughly equal to the drift time, $M_d \approx 4 \times 10^{22} (r/1 \text{ km}) \text{ g}$. Setting this mass equal to the equilibrium mass of solids in eq. 5 allows us to derive the input rate of solids, \dot{M}_0 , which generates a gas+solid configuration where the collision time is comparable to the drift time. This rate is rather large, $\sim 3 \times 10^{17} \text{ g s}^{-1}$. At this rate, the particle size with the maximum drift velocity is roughly 1 km. The much smaller accretion rates observed in metallic line white dwarfs precludes this option.

We conclude that gas drag has little impact on the evolution of the collisional cascade. For reasonable \dot{M}_0 , the collision time is always much shorter than the radial drift time. The physical conditions that allow the drift time to be comparable to the collision time are very unlikely.

4.6. Contacts with Observations

In KB2017 and this paper, we have considered collisional cascades as a plausible mechanism to place metals in white dwarf photospheres. However, the lack of robust delivery mechanisms and the simplicity of our initial calculations limit our ability to explain existing observations. As in KB2017, we list several points of contact between current data and theoretical predictions.

- Circumstellar gas has now been observed in a reasonably large sample of metallic line white dwarfs (e.g. Gänsicke et al. 2006, 2007, 2008; Melis et al. 2010; Farihi et al. 2012; Melis et al. 2012; Debes et al. 2012a; Wilson et al. 2014; Manser et al. 2016b; Hartmann et al. 2016; Manser et al. 2016a; Xu et al. 2016; Li et al. 2017; Redfield et al. 2017;

Melis & Dufour 2017). In some cases, the data place limits on the surface density of the gas (Hartmann et al. 2016). Although other models match the observations (e.g., Metzger et al. 2012), cascades with $\dot{M}_0 \approx 10^9 - 10^{11}$ routinely achieve the observed surface densities.

- Among systems with repeat observations, variable emission (absorption) features in the gas are common (rare) (e.g., Wilson et al. 2014; Manser et al. 2016b,a; Redfield et al. 2017; Melis & Dufour 2017, and references therein). On one occasion, features appear and then slowly fade over time scales of months to years. More often, consistently visible features vary on short time scales. In the cascade picture, occasional large-scale collisions can generate a gaseous disk which fades from view before the next collision replenishes the disk. During the peak of a cascade, short-term variations in Σ_g result from stochastic variations in the vaporization rate.
- In any cascade model, large Σ_g and \dot{M}_\star correlate with large M_d and significant IR excesses. Observations appear to support this correlation (e.g., Manser et al. 2016a). More comprehensive cascade calculations should allow more robust predictions for comparisons with existing data.
- Contrary to our assumptions, current observations indicate that gaseous disks are not axisymmetric. Large collision events among the solids are not axisymmetric; proper treatment of the vapor generated in these collisions might produce gaseous structures similar to those observed.
- X-ray observations provide an interesting window into the transport of material from the Roche limit to the white dwarf photosphere. From our calculations, we expect (i) fairly steady X-ray sources when \dot{M}_v and \dot{M}_\star are nearly constant in time and (ii) dramatically variable X-ray sources when r_0 is large and \dot{M}_0 is small (or variable). Unless the incoming gas is channeled by a magnetic field, both sets of objects should display the characteristic ‘flickering’ of accreting systems (e.g., Sokoloski & Kenyon 2003; Maoz et al. 2015). Although constraints on the X-ray luminosities of metallic line white dwarfs are limited (e.g., Farihi et al. 2017b; Rappaport et al. 2017, and references therein), there are some single white dwarfs with hard X-rays of unknown origin (e.g., Chu et al. 2004; Bilíková et al. 2010). Coupled with good limits on emission from an IR excess and circumstellar gas, broader surveys for X-ray emission among metallic line white dwarfs provide strong tests of theoretical models.

5. SUMMARY

We consider the evolution of a gaseous disk fed by a collisional cascade of solids orbiting within a narrow ring at the Roche limit of a low-mass white dwarf. In our picture, solids with radius r_0 , eccentricity $e_0 = 0.01$, and inclination $i_0 = e_0/2$ arrive in the ring at a rate \dot{M}_0 . Once the mass in solids reaches a critical level, destructive collisions fuel a collisional cascade which grinds the solids into $1 \mu\text{m}$ particles. Rapid vaporization of these small grains produces a ring of metallic gas coincident with the ring of solids. As the cascade continues, the ring of gas expands into a disk which extends from the surface of the white dwarf out past the Roche limit. The disk transports metals originally in the solids onto the white dwarf photosphere.

The evolution of the gaseous disk depends on the properties of the solids (r_0 and \dot{M}_0) and the properties of the gas (α , the viscosity parameter, and T_g , the gas temperature). Systems with $\dot{M}_0 \gtrsim \dot{M}_{0,crit} \approx 3 \times 10^4 (r_0/1 \text{ km})^{3.92} \text{ g s}^{-1}$ find a steady equilibrium state where the vaporization rate \dot{M}_v equals \dot{M}_0 . Once the ring of gas spreads into an extended disk, \dot{M}_\star , the accretion rate from the disk onto the central star, is roughly 90% of \dot{M}_0 . With a nearly constant rate of mass flow through the disk, the surface density at any distance from the central star scales inversely with α and T_g .

When \dot{M}_0 is smaller, $\lesssim \dot{M}_{0,crit}$, it takes a long time for the ring to collect enough solids to begin the collisional cascade. During this low state, the vaporization rate \dot{M}_v and \dot{M}_\star are much much smaller than \dot{M}_0 . Once the collisional cascade begins, \dot{M}_v and (somewhat later) \dot{M}_\star grow very rapidly. During the most intense part of the cascade, \dot{M}_v and \dot{M}_\star become much larger than \dot{M}_0 . The mass in solids then slowly decreases, reducing \dot{M}_v and \dot{M}_\star . Eventually, the cascade ceases; \dot{M}_v and \dot{M}_\star drop precipitously. As long as the ring continues to accrete solids at some low rate, the cycle of low and high states repeats.

When a system oscillates between low and high states, α and T_g set the time scales (i) for the newly-formed ring of gas to spread into a disk at the start of the cascade, and (ii) for the extended disk of gas to drain onto the central star when the cascade ends. The time scale for a ring of gas near the Roche limit to spread to the stellar photosphere is roughly $\tau_s \approx 10^3 (10^{-3}/\alpha) (1500 \text{ K}/T_0) \text{ yr}$; the draining time is 5–10 times the spreading time.

As in our previous calculations, the vertical scale height of the solids remains large throughout the cascade. A revised analysis demonstrates that gas drag has little impact on the evolution of the solids. Together with results in KB2017, it seems unlikely that some combination of collisional, gas dynamical, or radiative processes can reduce the vertical scale height of the solids, $H \approx 10^8 - 10^9 \text{ cm}$, to levels required in the Jura (2003) model, $H \approx 100\text{--}1000 \text{ cm}$.

Aside from ultraviolet, optical, and infrared spectroscopy, X-ray fluxes provide strong constraints on theoretical models for gaseous disks in metallic line white dwarfs. In systems where r_0 and \dot{M}_0 vary with time, we expect occasional bright states with $L_X/L_\odot \gtrsim 10^{-5}$ and long-lived faint states with much smaller L_X/L_\odot . By analogy with cataclysmic variables, the X-ray temperature during the high state depends on the geometry and optical depth of the accreting material (e.g., Mukai 2017, and references therein). Deep surveys with existing (e.g. Bilíková et al. 2010; Kastner et al. 2012, and references therein) and planned (e.g., Predehl 2014) X-ray facilities can test these ideas.

We acknowledge generous allotments of computer time on the NASA ‘discover’ cluster. We thank J. Farihi, M. Geller, M. Payne, S. Rappaport, A. Vanderburg, and D. Veras for advice, comments, and encouragement. Comments from an anonymous referee greatly improved our presentation. Portions of this project were supported by the *NASA Outer Planets* and *Emerging Worlds* programs through grants NNX11AM37G and NNX17AE24G.

REFERENCES

- Adachi, I., Hayashi, C., & Nakazawa, K. 1976, *Progress of Theoretical Physics*, 56, 1756
- Alcock, C., Fristrom, C. C., & Siegelman, R. 1986, *ApJ*, 302, 462
- Alcock, C., & Illarionov, A. 1980, *ApJ*, 235, 541
- Antoniadou, K. I., & Veras, D. 2016, *MNRAS*, 463, 4108
- Barber, S. D., Kilic, M., Brown, W. R., & Gianninas, A. 2014, *ApJ*, 786, 77
- Barber, S. D., Patterson, A. J., Kilic, M., et al. 2012, *ApJ*, 760, 26
- Bath, G. T., & Pringle, J. E. 1981, *MNRAS*, 194, 967
- . 1982, *MNRAS*, 199, 267
- Bear, E., & Soker, N. 2013, *New A*, 19, 56
- Bergfors, C., Farihi, J., Dufour, P., & Rocchetto, M. 2014, *MNRAS*, 444, 2147
- Bilíková, J., Chu, Y.-H., Gruendl, R. A., & Maddox, L. A. 2010, *AJ*, 140, 1433
- Bochkarev, K. V., & Rafikov, R. R. 2011, *ApJ*, 741, 36
- Bonsor, A., Farihi, J., Wyatt, M. C., & van Lieshout, R. 2017, *MNRAS*, 468, 154
- Bonsor, A., Mustill, A. J., & Wyatt, M. C. 2011, *MNRAS*, 414, 930
- Bonsor, A., & Veras, D. 2015, *MNRAS*, 454, 53
- Bromley, B. C., & Kenyon, S. J. 2011a, *ApJ*, 731, 101
- . 2011b, *ApJ*, 735, 29
- . 2013, *ApJ*, 764, 192
- Bromley, B. C., Kenyon, S. J., Geller, M. J., & Brown, W. R. 2012, *ApJ*, 749, L42
- Brown, J. C., Veras, D., & Gaensicke, B. T. 2017, *MNRAS*, 468, 1575
- Burns, J. A., Lamy, P. L., & Soter, S. 1979, *Icarus*, 40, 1
- Caiazzo, I., & Heyl, J. S. 2017, *MNRAS*, 469, 2750
- Cannizzo, J. K., Lee, H. M., & Goodman, J. 1990, *ApJ*, 351, 38

- Cannizzo, J. K., & Wheeler, J. C. 1984, *ApJS*, 55, 367
- Chu, Y.-H., Guerrero, M. A., Gruendl, R. A., & Webbink, R. F. 2004, *AJ*, 127, 477
- Chu, Y.-H., Su, K. Y. L., Bilikova, J., et al. 2011, *AJ*, 142, 75
- Cottrell, P. L., & Greenstein, J. L. 1980, *ApJ*, 242, 195
- D’Alessio, P., Canto, J., Calvet, N., & Lizano, S. 1998, *ApJ*, 500, 411
- Debes, J. H., Hoard, D. W., Wachter, S., Leisawitz, D. T., & Cohen, M. 2011, *ApJS*, 197, 38
- Debes, J. H., Kilic, M., Faedi, F., et al. 2012a, *ApJ*, 754, 59
- Debes, J. H., & Sigurdsson, S. 2002, *ApJ*, 572, 556
- Debes, J. H., Walsh, K. J., & Stark, C. 2012b, *ApJ*, 747, 148
- Dong, R., Wang, Y., Lin, D. N. C., & Liu, X.-W. 2010, *ApJ*, 715, 1036
- Farihi, J. 2016, *New A Rev.*, 71, 9
- Farihi, J., Gänsicke, B. T., Steele, P. R., et al. 2012, *MNRAS*, 421, 1635
- Farihi, J., Jura, M., & Zuckerman, B. 2009, *ApJ*, 694, 805
- Farihi, J., von Hippel, T., & Pringle, J. E. 2017a, *MNRAS*, 471, L145
- Farihi, J., Fossati, L., Wheatley, P. J., et al. 2017b, *ArXiv e-prints*, arXiv:1709.08206
- Frewen, S. F. N., & Hansen, B. M. S. 2014, *MNRAS*, 439, 2442
- Gänsicke, B. T., Koester, D., Marsh, T. R., Rebassa-Mansergas, A., & Southworth, J. 2008, *MNRAS*, 391, L103
- Gänsicke, B. T., Marsh, T. R., & Southworth, J. 2007, *MNRAS*, 380, L35
- Gänsicke, B. T., Marsh, T. R., Southworth, J., & Rebassa-Mansergas, A. 2006, *Science*, 314, 1908
- Gezari, S., Heckman, T., Cenko, S. B., et al. 2009, *ApJ*, 698, 1367
- Ghosh, P., & Lamb, F. K. 1979, *ApJ*, 232, 259
- Girven, J., Gänsicke, B. T., Steeghs, D., & Koester, D. 2011, *MNRAS*, 417, 1210

- Hamers, A. S., & Portegies Zwart, S. F. 2016, *MNRAS*, 462, L84
- Hansen, B. M. S., Kulkarni, S., & Wiktorowicz, S. 2006, *AJ*, 131, 1106
- Hartmann, S., Nagel, T., Rauch, T., & Werner, K. 2016, *A&A*, 593, A67
- Hoard, D. W., Debes, J. H., Wachter, S., Leisawitz, D. T., & Cohen, M. 2013, *ApJ*, 770, 21
- Holsapple, K. A., & Michel, P. 2006, *Icarus*, 183, 331
- . 2008, *Icarus*, 193, 283
- Ida, S., & Lin, D. N. C. 2008, *ApJ*, 673, 487
- Jura, M. 2003, *ApJ*, 584, L91
- . 2008, *AJ*, 135, 1785
- Jura, M., Farihi, J., & Zuckerman, B. 2007a, *ApJ*, 663, 1285
- Jura, M., Farihi, J., Zuckerman, B., & Becklin, E. E. 2007b, *AJ*, 133, 1927
- Jura, M., & Young, E. D. 2014, *Annual Review of Earth and Planetary Sciences*, 42, 45
- Kastner, J. H., Montez, Jr., R., Balick, B., et al. 2012, *AJ*, 144, 58
- Kennedy, G. M., & Kenyon, S. J. 2008, *ApJ*, 673, 502
- Kenyon, S. J., & Bromley, B. C. 2001, *AJ*, 121, 538
- . 2004, *AJ*, 127, 513
- . 2008, *ApJS*, 179, 451
- . 2015a, *ApJ*, 806, 42
- . 2015b, *ApJ*, 811, 60
- . 2016, *ApJ*, 817, 51
- . 2017, *ApJ*, 844, 116
- Kenyon, S. J., Najita, J. R., & Bromley, B. C. 2016, *ApJ*, 831, 8
- Kenyon, S. J., Shipman, H. L., Sion, E. M., & Aannestad, P. A. 1988, *ApJ*, 328, L65
- Kepler, S. O., Pelisoli, I., Koester, D., et al. 2016, *MNRAS*, 455, 3413

- Kilic, M., von Hippel, T., Leggett, S. K., & Winget, D. E. 2005, *ApJ*, 632, L115
- King, A. R., Pringle, J. E., & Livio, M. 2007, *MNRAS*, 376, 1740
- Kochanek, C. S. 2016, *MNRAS*, 461, 371
- Koester, D., Gänsicke, B. T., & Farihi, J. 2014, *A&A*, 566, A34
- Koester, D., & Wilken, D. 2006, *A&A*, 453, 1051
- Kotko, I., & Lasota, J.-P. 2012, *A&A*, 545, A115
- Kuulkers, E., Norton, A., Schwobe, A., & Warner, B. 2006, in *Compact stellar X-ray sources*, ed. W. H. G. Lewin & M. van der Klis (Cambridge University Press, Cambridge, UK), 421–460
- Lacombe, P., Wesemael, F., Fontaine, G., & Liebert, J. 1983, *ApJ*, 272, 660
- Li, J., Ferrario, L., & Wickramasinghe, D. 1998, *ApJ*, 503, L151
- Li, L., Zhang, F., Kong, X., Han, Q., & Li, J. 2017, *ApJ*, 836, 71
- Liebert, J., Wehrse, R., & Green, R. F. 1987, *A&A*, 175, 173
- Lodato, G., & Rossi, E. M. 2011, *MNRAS*, 410, 359
- Lynden-Bell, D., & Pringle, J. E. 1974, *MNRAS*, 168, 603
- Lyra, W., Paardekooper, S.-J., & Mac Low, M.-M. 2010, *ApJ*, 715, L68
- Malamud, U., & Perets, H. B. 2016, *ApJ*, 832, 160
- . 2017a, *ApJ*, 842, 67
- . 2017b, ArXiv e-prints, arXiv:1708.07489
- Manser, C. J., Gänsicke, B. T., Koester, D., Marsh, T. R., & Southworth, J. 2016a, *MNRAS*, 462, 1461
- Manser, C. J., Gänsicke, B. T., Marsh, T. R., et al. 2016b, *MNRAS*, 455, 4467
- Maoz, D., Mazeh, T., & McQuillan, A. 2015, *MNRAS*, 447, 1749
- Masset, F. S., & Papaloizou, J. C. B. 2003, *ApJ*, 588, 494
- Melis, C., & Dufour, P. 2017, *ApJ*, 834, 1

- Melis, C., Jura, M., Albert, L., Klein, B., & Zuckerman, B. 2010, *ApJ*, 722, 1078
- Melis, C., Dufour, P., Farihi, J., et al. 2012, *ApJ*, 751, L4
- Metzger, B. D., Rafikov, R. R., & Bochkarev, K. V. 2012, *MNRAS*, 423, 505
- Meyer, F., & Meyer-Hofmeister, E. 1982, *A&A*, 106, 34
- Mineshige, S., & Osaki, Y. 1983, *PASJ*, 35, 377
- Mukai, K. 2017, *PASP*, 129, 062001
- Mustill, A. J., Veras, D., & Villaver, E. 2014, *MNRAS*, 437, 1404
- Najita, J. R., Ádámkóvics, M., & Glassgold, A. E. 2011, *ApJ*, 743, 147
- Najita, J. R., Carr, J. S., Pontoppidan, K. M., et al. 2013, *ApJ*, 766, 134
- Nelson, R. P., & Papaloizou, J. C. B. 2004, *MNRAS*, 350, 849
- Parriott, J., & Alcock, C. 1998, *ApJ*, 501, 357
- Payne, M. J., Veras, D., Gänsicke, B. T., & Holman, M. J. 2017, *MNRAS*, 464, 2557
- Payne, M. J., Veras, D., Holman, M. J., & Gänsicke, B. T. 2016, *MNRAS*, 457, 217
- Petrovich, C., & Muñoz, D. J. 2017, *ApJ*, 834, 116
- Predehl, P. 2014, *Astronomische Nachrichten*, 335, 517
- Press, W. H., Teukolsky, S. A., Vetterling, W. T., & Flannery, B. P. 1992, *Numerical recipes in FORTRAN. The art of scientific computing* (Cambridge: Cambridge University Press)
- Pretorius, M. L., & Knigge, C. 2012, *MNRAS*, 419, 1442
- Pringle, J. E. 1981, *ARA&A*, 19, 137
- Rafikov, R. R. 2011a, *ApJ*, 732, L3
- . 2011b, *MNRAS*, 416, L55
- Rafikov, R. R., & Garmilla, J. A. 2012, *ApJ*, 760, 123
- Rappaport, S., Gary, B. L., Vanderburg, A., et al. 2017, *ArXiv e-prints*, arXiv:1709.08195
- Reach, W. T., Kuchner, M. J., von Hippel, T., et al. 2005, *ApJ*, 635, L161

- Redfield, S., Farihi, J., Cauley, P. W., et al. 2017, *ApJ*, 839, 42
- Rees, M. J. 1988, *Nature*, 333, 523
- Reis, R. C., Wheatley, P. J., Gänsicke, B. T., & Osborne, J. P. 2013, *MNRAS*, 430, 1994
- Rocchetto, M., Farihi, J., Gänsicke, B. T., & Bergfors, C. 2015, *MNRAS*, 449, 574
- Shipman, H. L., & Greenstein, J. L. 1983, *ApJ*, 266, 761
- Shipman, H. L., Greenstein, J. L., & Boksenberg, A. 1977, *AJ*, 82, 480
- Sion, E. M., Kenyon, S. J., & Aannestad, P. A. 1990, *ApJS*, 72, 707
- Smak, J. 1999, *Acta Astron.*, 49, 391
- Sokoloski, J. L., & Kenyon, S. J. 2003, *ApJ*, 584, 1027
- Stephan, A. P., Naoz, S., & Zuckerman, B. 2017, *ApJ*, 844, L16
- Stern, S. A., Shull, J. M., & Brandt, J. C. 1990, *Nature*, 345, 305
- Takeuchi, T., & Artymowicz, P. 2001, *ApJ*, 557, 990
- Tanaka, H., Takeuchi, T., & Ward, W. R. 2002, *ApJ*, 565, 1257
- Tremblay, P.-E., & Bergeron, P. 2007, *ApJ*, 657, 1013
- Veras, D. 2016, *Royal Society Open Science*, 3, 150571
- Veras, D., Carter, P. J., Leinhardt, Z. M., & Gänsicke, B. T. 2017, *MNRAS*, 465, 1008
- Veras, D., Eggl, S., & Gänsicke, B. T. 2015a, *MNRAS*, 452, 1945
- . 2015b, *MNRAS*, 451, 2814
- Veras, D., & Gänsicke, B. T. 2015, *MNRAS*, 447, 1049
- Veras, D., Leinhardt, Z. M., Bonsor, A., & Gänsicke, B. T. 2014a, *MNRAS*, 445, 2244
- Veras, D., Mustill, A. J., Bonsor, A., & Wyatt, M. C. 2013, *MNRAS*, 431, 1686
- Veras, D., Shannon, A., & Gänsicke, B. T. 2014b, *MNRAS*, 445, 4175
- Villaver, E., & Livio, M. 2007, *ApJ*, 661, 1192
- von Hippel, T., Kuchner, M. J., Kilic, M., Mullally, F., & Reach, W. T. 2007, *ApJ*, 662, 544

- Ward, W. R. 1997, *Icarus*, 126, 261
- Weidenschilling, S. J. 1977, *MNRAS*, 180, 57
- Wilson, D. J., Gänsicke, B. T., Koester, D., et al. 2014, *MNRAS*, 445, 1878
- Wyatt, M. C., Farihi, J., Pringle, J. E., & Bonsor, A. 2014, *MNRAS*, 439, 3371
- Xu, S., Jura, M., Dufour, P., & Zuckerman, B. 2016, *ApJ*, 816, L22
- Xu, S., Zuckerman, B., Dufour, P., et al. 2017, *ApJ*, 836, L7
- Youdin, A. N. 2010, in *EAS Publications Series*, Vol. 41, *EAS Publications Series*, ed. T. Montmerle, D. Ehrenreich, & A.-M. Lagrange, 187–207
- Youdin, A. N., & Chiang, E. I. 2004, *ApJ*, 601, 1109
- Youdin, A. N., & Kenyon, S. J. 2013, *From Disks to Planets*, ed. T. D. Oswalt, L. M. French, & P. Kalas (Dordrecht: Springer Science & Business Media), 1
- Zuckerman, B., & Reid, I. N. 1998, *ApJ*, 505, L143

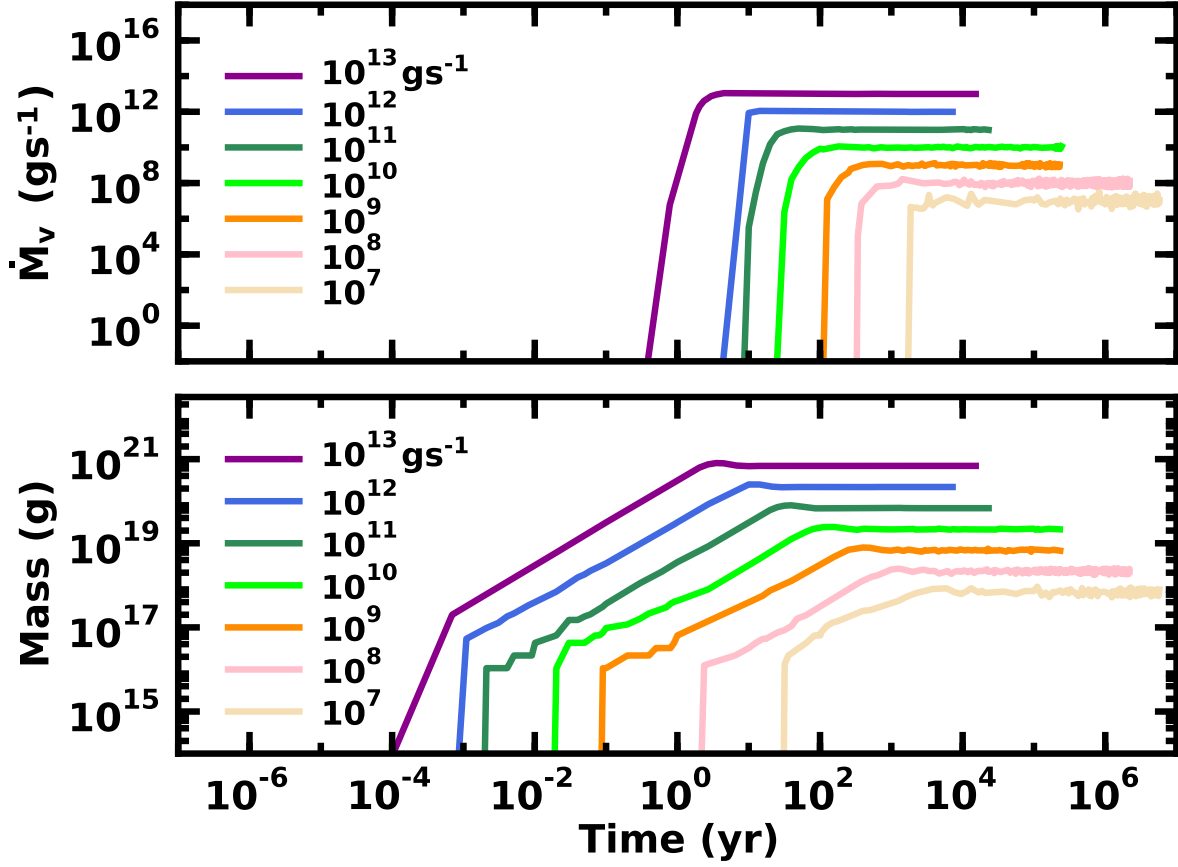


Fig. 1.— Time evolution of the mass in solids M_d (lower panel) and the mass vaporization rate \dot{M}_v (upper panel) for calculations with $r_0 = 1$ km and the mass input rates (\dot{M}_0) indicated in the legend. In each calculation, the mass grows roughly linearly in time from zero to a constant level. During this increase, the collisional cascade begins; the vaporization rate (equivalently the production rate of particles with $r \lesssim 1 \mu\text{m}$) grows abruptly and then reaches a roughly constant level. A balance between the input rate and the vaporization rate maintains a constant mass in the annulus.

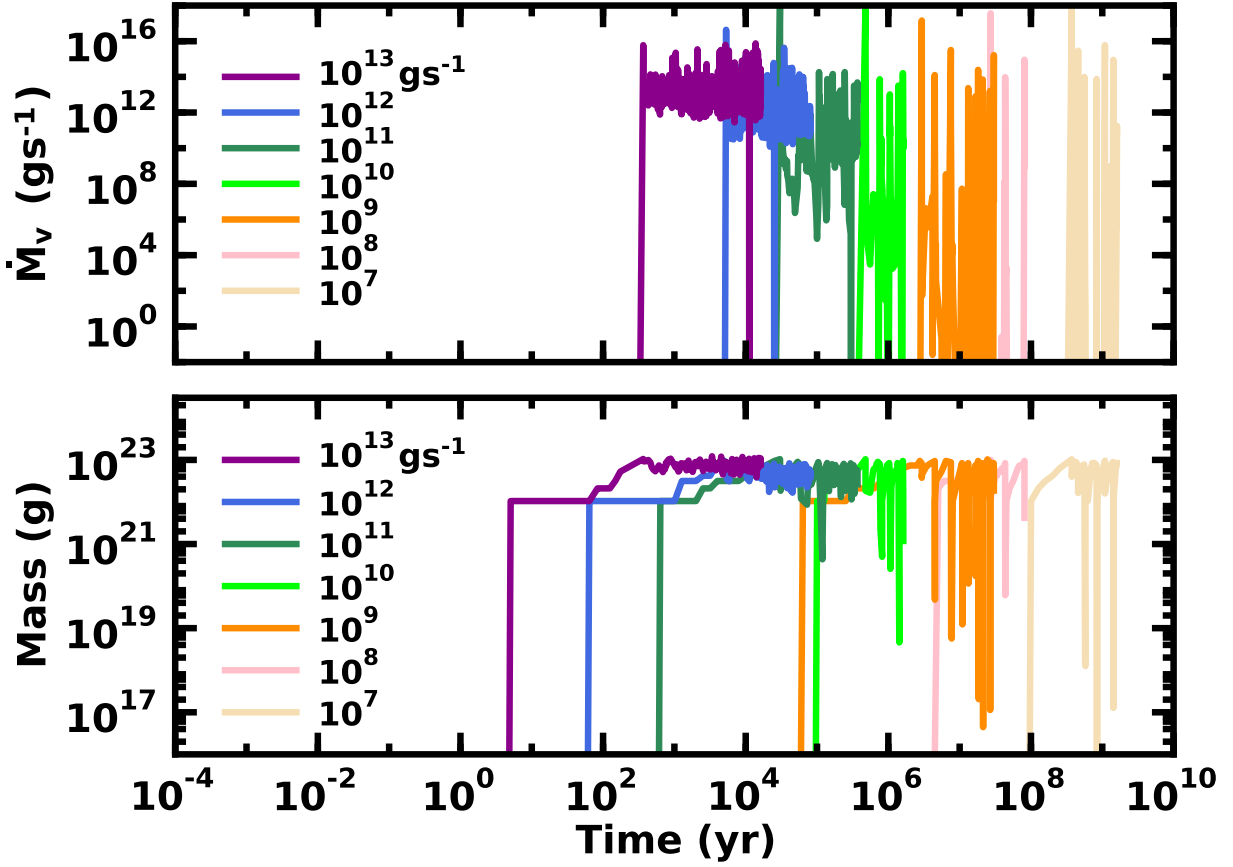


Fig. 2.— As in Fig. 1 for calculations with $r_0 = 100$ km. In these calculations, the mass and vaporization rate either maintain a roughly constant level (for large \dot{M}_0) or oscillate between low and high states (for small \dot{M}_0).

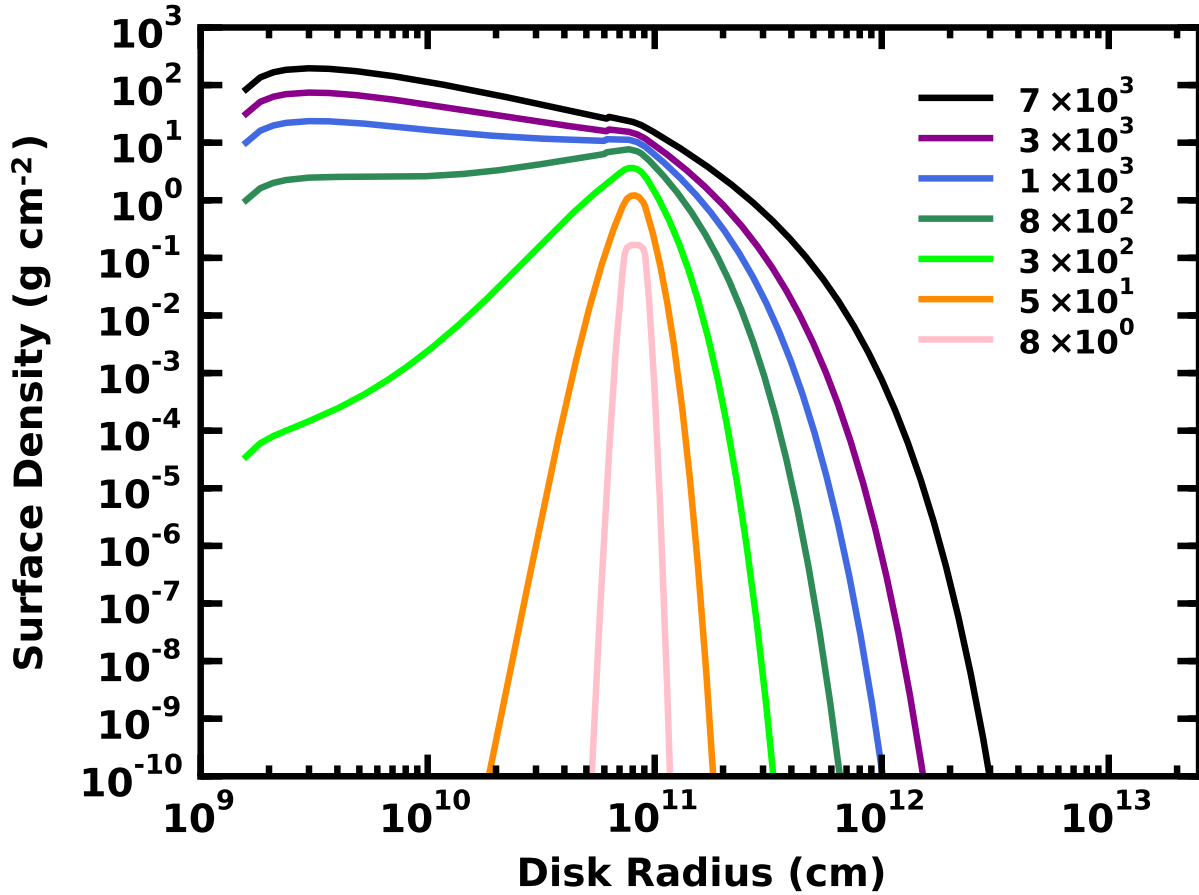


Fig. 3.— Snapshots of $\Sigma_g(a)$ for a gaseous disk fed by solids from a collisional cascade with $r_0 = 1$ km and $\dot{M}_0 = 10^{13}$ g s $^{-1}$. The legend indicates times (in yr) for each snapshot. At 5–10 yr, a gaseous ring is roughly centered on the annulus of solids at $a = 1.16 R_\odot$. As the cascade adds more material to the ring, it expands. After 200–300 yr, material begins to reach the surface of the white dwarf. As the surface density grows at the inner edge of the disk, material expands well beyond the Roche limit and reaches $a \approx 10\text{--}20 R_\odot$ in 10^4 yr.

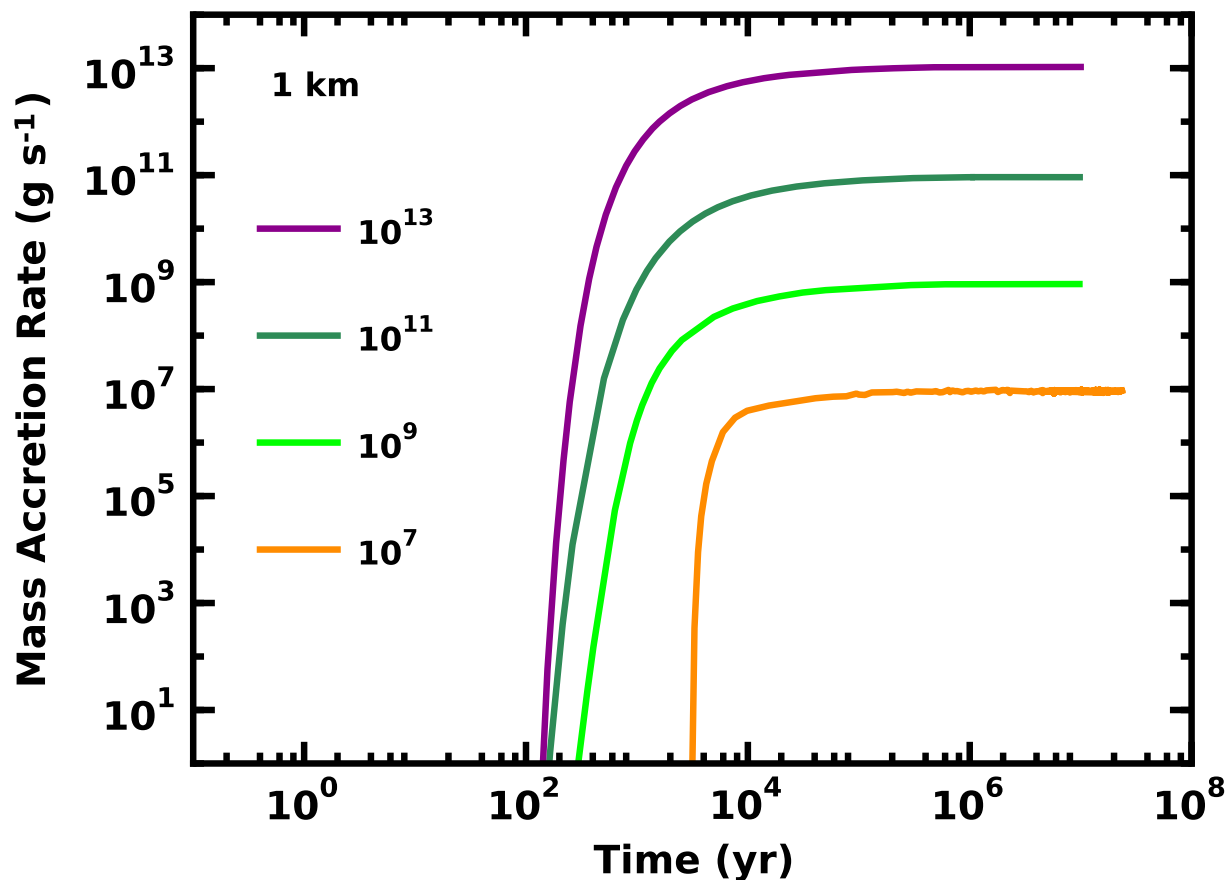


Fig. 4.— Time evolution of \dot{M}_* , the accretion rate onto the central white dwarf, during a collisional cascade. Solids with radius $r_0 = 1$ km are added to an annulus near the Roche limit at rates indicated in the legend. Destructive collisions grind the solids into $1 \mu\text{m}$ particles. Radiation from the central star vaporizes these small particles; the resulting gas is added to an annulus within a circumstellar disk. Once the collisional cascade develops, the accretion rate onto the white dwarf smoothly increases. As the evolution proceeds, the accretion rate onto the white dwarf approaches the input rate for solids at the Roche limit.

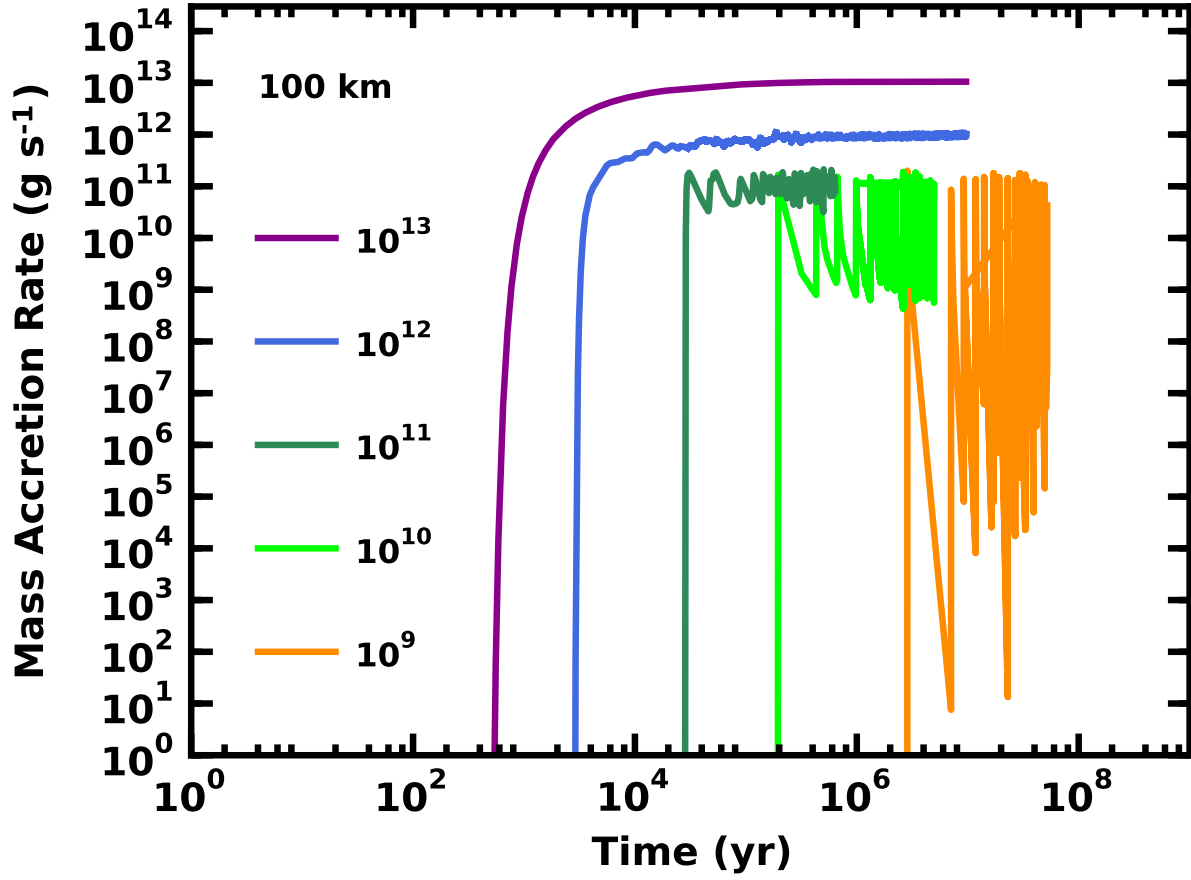


Fig. 5.— As in Fig. 4 for $r_0 = 100$ km. For large input rates of solids, $\dot{M}_0 \gtrsim 3 \times 10^{11}$ g s⁻¹, the accretion rate onto the white dwarf is fairly constant in time. At smaller rates, the accretion rate onto the white dwarf varies dramatically.

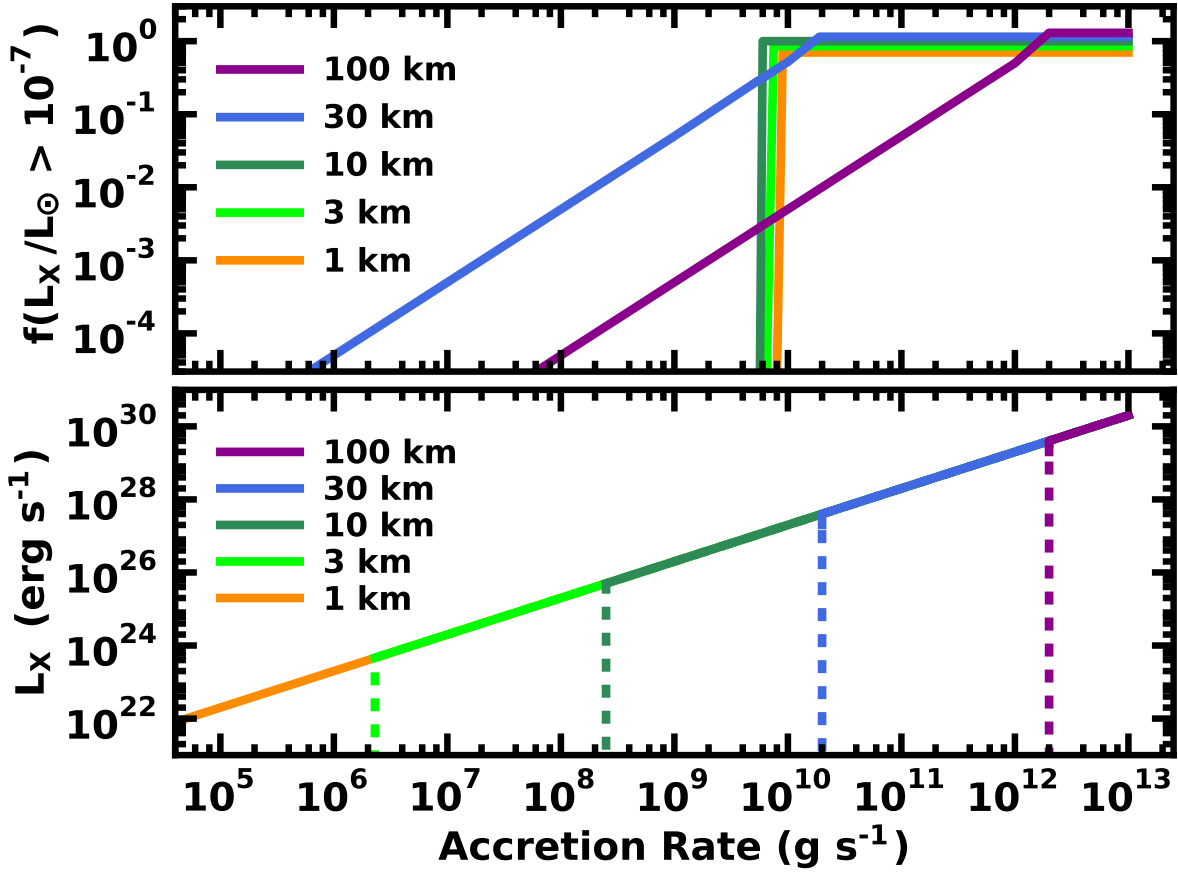


Fig. 6.— Predictions for the X-ray luminosity L_X of metallic line white dwarfs accreting from a viscous disk fed by a collisional cascade. *Lower panel:* L_X as a function of \dot{M}_0 for $r_0 = 1$ –100 km as indicated in the legend. Solid (dashed) lines indicate regimes where the collisional cascade and accretion onto the white dwarf are steady (intermittent). *Upper panel:* Predicted fraction of time accreting white dwarfs spend with $L_X/L_\odot > 10^{-7}$ as a function of \dot{M}_0 and r_0 . For clarity, some predicted values have been displaced vertically or horizontally. Systems with $r_0 \lesssim 10$ km have no episodic evolution and spend all of their time with a fraction of zero or unity. Episodic evolution in systems with $r_0 \gtrsim 30$ km produces a broader range of accretion luminosities for an input \dot{M}_0 .

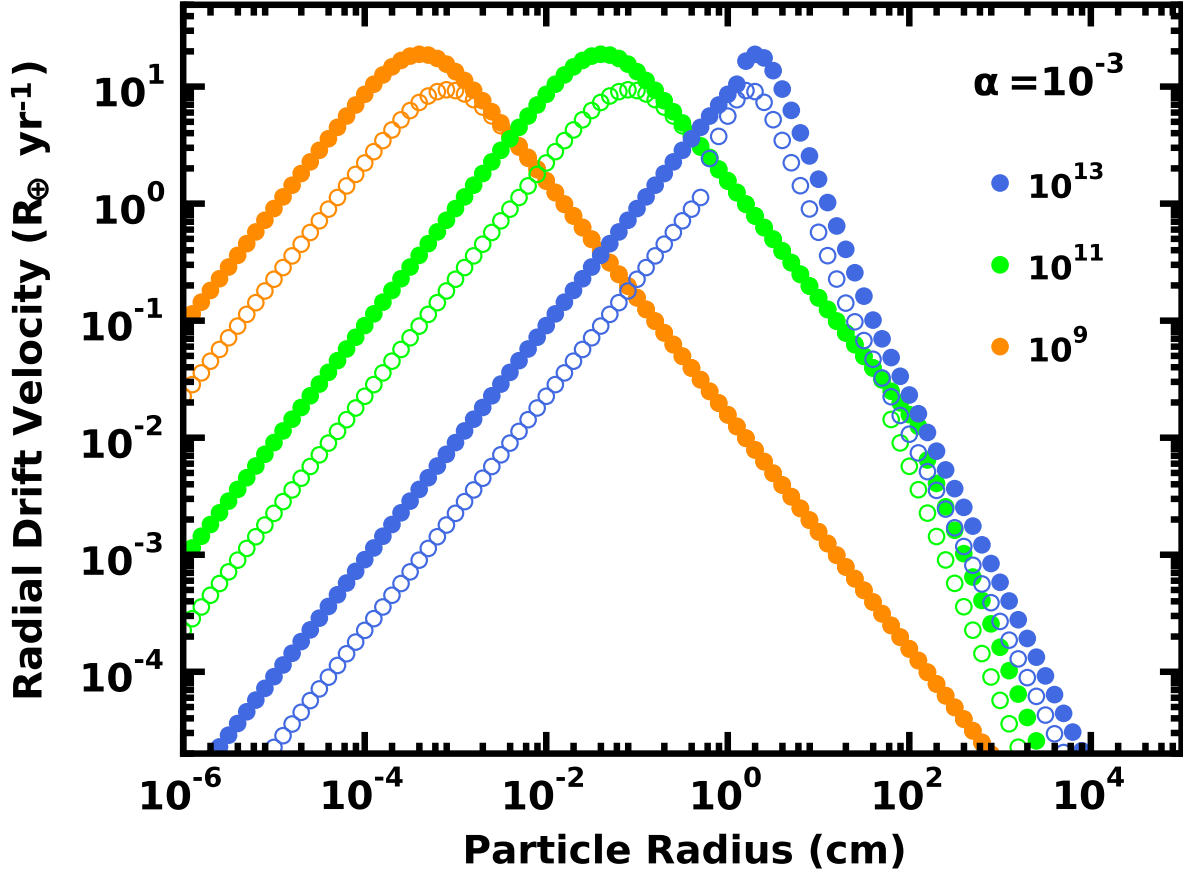


Fig. 7.— Radial drift velocity as a function of particle size for solids at $a_0 = 1.15 R_\odot$ within a steady-state gaseous disk generated by vaporization of $1 \mu\text{m}$ and smaller particles. The legend indicates the input \dot{M}_0 in solids and the α for the gas. Particles in disks with $T_0 = 1500 \text{ K}$ (open circles) have somewhat smaller radial drift velocity than those in disks with $T_0 = 3000 \text{ K}$ (filled circles). At the maximum radial drift velocity of 5 (10) $R_\oplus \text{ yr}^{-1}$ for $T_0 = 1500 \text{ K}$ ($T_0 = 3000 \text{ K}$), the collisional cascade destroys small solid particles before radial drift removes them from the annulus.

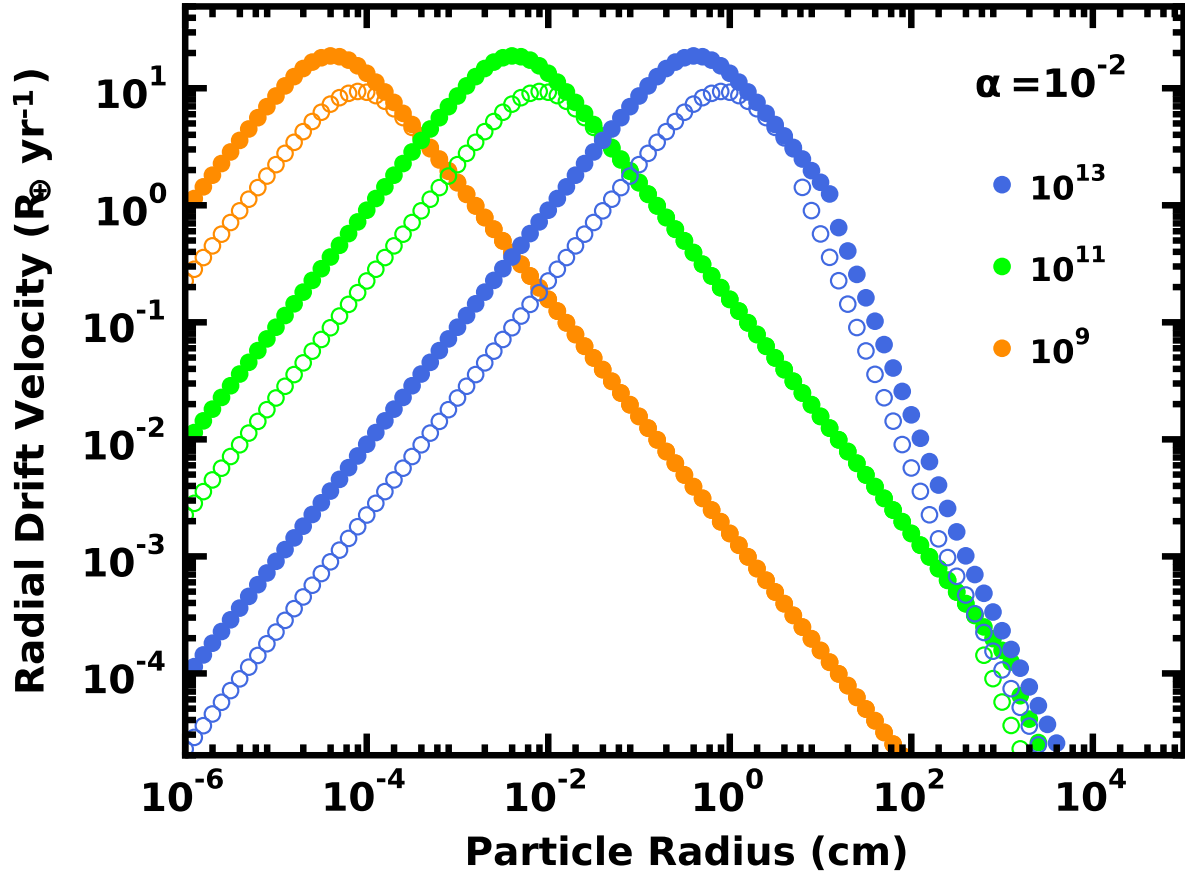


Fig. 8.— As in Fig. 7 for disks $\alpha = 10^{-2}$. Disks with larger α have smaller Σ_g . Although the maximum drift velocity is independent of α , smaller particles have the maximum drift velocity when α is larger.